

UNI-NTFM: A UNIFIED FOUNDATION MODEL FOR EEG SIGNAL REPRESENTATION LEARNING

Zhisheng Chen^{1,2}, Yingwei Zhang^{1,2}, Qizhen Lan³, Tianyu Liu⁴, Huacan Wang², Yi Ding⁵, Ziyu Jia⁶, Ronghao Chen⁷, Kun Wang⁵ & Xinliang Zhou⁵

¹Beijing Key Laboratory of Mobile Computing and Pervasive Device, Institute of Computing Technology, Chinese Academy of Sciences ²University of the Chinese Academy of Sciences

³University of Alabama at Birmingham ⁴The University of Hong Kong ⁵College of Computing and Data Science, Nanyang Technological University ⁶Institute of Automation, Chinese Academy of Sciences ⁷Peking University

chenzhisheng25@mails.ucas.ac.cn, zhangyingwei@ict.ac.cn
qlan@uab.edu, liu_ty@stu.xjtu.edu.cn, wanghuacan17@mails.ucas.ac.cn
ding.yi@ntu.edu.sg, jia.ziyu@outlook.com
chenronghao@alumni.pku.edu.cn, wk520529wjh@gmail.com
xinliang001@e.ntu.edu.sg

ABSTRACT

Foundation models pretrained on various and unlabeled data have demonstrated significant success in natural language and vision, but their application to electroencephalography (EEG) remains challenged due to the signal’s unique properties. Existing brain foundation models that inherit architectures designed for text or images lead to three limitations in pre-training: 1) conflating time-domain waveform patterns with frequency-domain rhythmic features in a single processing stream, 2) ignoring the critical spatial topology of electrodes with different standards, and 3) reliance on the inflexible, dense network to process functionally distinct EEG patterns. To address these challenges, we introduce the **Unified Neural Topological Foundation Model (Uni-NTFM)**, which is designed based on neuroscience principles to produce universal and interpretable representations. Uni-NTFM integrates three core innovations: 1) a decoupled architecture parallelly encodes time, frequency, and raw signal representations before performing cross-domain feature integration; 2) a topological embedding mechanism to unify electrodes from different international standards and generate structured input sequences for brain regions; and 3) a Mixture-of-Experts neural Transformer that efficiently scales model capacity by routing signal patterns to specialized subnetworks. The largest model, Uni-NTFM_{large}, has a record-breaking 1.9B parameters and was pretrained on over 28,000 hours of diverse EEG data via a dual-domain masked reconstruction objective. Uni-NTFM significantly outperforms existing task-specific methods and foundation models across nine distinct downstream tasks under both linear probing and fine-tuning settings, demonstrating a superior ability to learn universal representations of brain activity. Our code is available at <https://anonymous.4open.science/r/Uni-NTFM-0924>.

1 INTRODUCTION

Electroencephalography (EEG), as an effective observational window with high temporal resolution, provides a critical technological means for real-time monitoring of brain activity, has indispensable value in fields such as clinical diagnosis, neuroscience research, and Brain-Computer Interfaces (BCIs) (Pfurtscheller & Neuper, 2001; Flesher et al., 2021; Ieracitano et al., 2019). However, with the increasing ability for data acquisition, researchers are confronted with complex and massively scaled EEG data. In this context, traditional task-specific modeling approaches, limited by their generalization capabilities, are no longer sufficient to fully uncover the universal neural encoding principles embedded within (Banville et al., 2021).

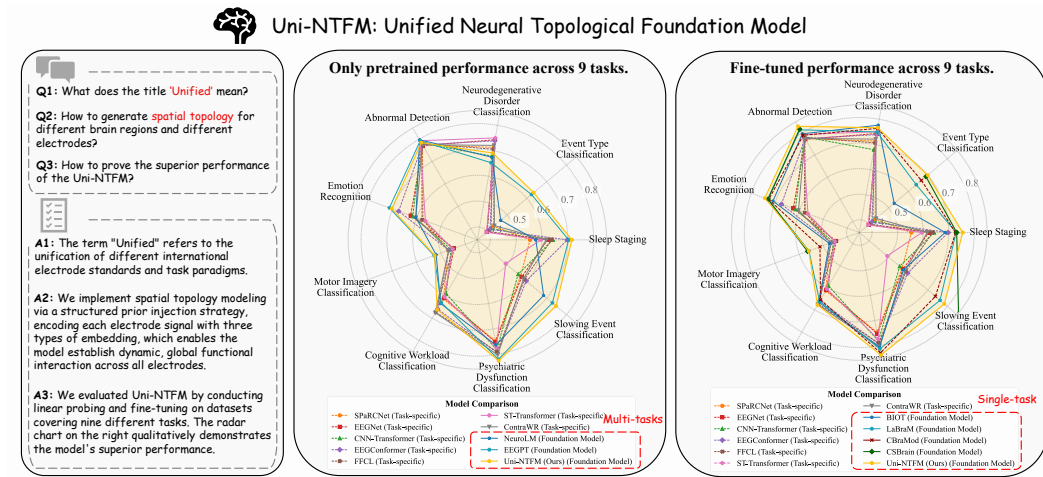


Figure 1: The overview of Uni-NTFM’s core concepts and superior performance. The left panel summarizes the model’s “Unified” principle, spatial topology strategy, and method of performance validation in a Q&A format. The two radar charts on the right demonstrate that Uni-NTFM comprehensively outperforms baseline models across nine distinct downstream tasks in both linear probing and fine-tuning settings.

Concurrently, the field of artificial intelligence has witnessed the success of the foundation model paradigm, which acquires general-purpose data representations through large-scale self-supervised learning. And this paradigm has achieved breakthrough progress in natural language processing and computer vision (Devlin et al., 2019; Radford et al., 2021; Kirillov et al., 2023; Achiam et al., 2023). Inspired by this, the researchers are actively exploring the migration of this paradigm to the EEG domain (Jiang et al., 2024a; Wang et al., 2024b). The goal is to fully unlock the potential of large-scale EEG data through self-supervised learning, thereby discovering universal neural representations and fundamentally elevating our understanding of the brain’s complex dynamics (Zhou et al., 2025a). The work related to brain foundation models (BFMs) is described in detail in Appendix A. However, current BFs largely inherit the general-purpose paradigm designed for language or vision: segmenting continuous signals into discrete, fixed-scale units (patches or tokens) and then employing a dense attention network for global information interaction. While this approach formally unifies the processing pipeline by directly transferring a model paradigm based on symbols and pixels to the physiological signal domain, its basic design philosophy contradicts the fundamental physical properties of EEG signals, thereby imposing limitations on the model’s representation ability. Specifically, existing brain foundation models face three core architectural challenges:

- 1) Confusion of Representations:** Models typically treat the EEG as a homogeneous time series and process in a single stream, which leads to mutual interference of representational abilities.
- 2) Absence of Spatial Topology and Electrode Unification:** Most models treat electrode channels as an unordered set or a simple sequence and only retain data from electrodes with identical names when confronted with different international standards. This leads to the loss of important spatial priors, making it difficult to learn functional connectivity patterns between brain regions.
- 3) Computational Bottlenecks in Model Scalability:** The reliance on a dense feed-forward network (FFN) architecture creates a significant computational bottleneck when scaling up model capacity, thereby limiting the efficiency of developing larger-scale models.
- 4) Lack of Specialized Modeling for Heterogeneous EEG Patterns:** EEG data is inherently a complex mixture of functionally distinct patterns, including normal rhythms, pathological waveforms, and diverse artifacts. The FFN-based Transformer struggles to perform the specialized modeling to capture the unique characteristics of each specific pattern as a single, universal processor.

In summary, existing models fundamentally lack an analysis of the intrinsic structure of EEG signals. Therefore, constructing a new architecture capable of synergistically modeling its temporal dynamics, spatial topology, and pattern-specific characteristics has become an imperative for the advancement of the field. As Figure 1, to address these challenges, we propose the **Unified Neural Topological Foundation Model (Uni-NTFM)**, a foundation model designed for generalized EEG decoding that is deeply aligned with the brain’s principles. We design a multi-domain and structure-aware information processing architecture that simulates 1) multi-domain perception, 2) cross-domain fusion, 3) higher-order cognition. Our core contributions are as follows:

- 1) **Decoupling and Synergy of Heterogeneous Features:** We designed a *Heterogeneous Feature Projection Module (HFPM)* with time, spectrum, and a lossless reference to achieve a physical decoupling of the multidimensional information in EEG. In addition, a *Dual-domain Cross-attention Module (DCM)* is established to achieve a synergistic dialogue between the time-domain and frequency-domain representations, generating a deeply fused representation through bidirectional information enhancement.
- 2) **Explicit and Unification Embedding of Spatial Topology:** Through a hierarchical *Topological Embedding (TE)* scheme comprising brain-region level, intra-region electrode level, and absolute sequence position level, we inject a precise neural coordinate system into channels from different datasets, enabling it to perceive and reveal the brain’s functional structure.
- 3) **Functionally MoE-based Neural Transformer:** We replace the traditional FFN with a *Mixture-of-Experts (MoE)* architecture. This design allows the model to dynamically route different signal patterns to functionally specialized expert subnetworks, and achieves fine-grained, specialized modeling of complex EEG components while efficiently scaling model capacity.
- 4) **Dual-domain Self-supervised Reconstruction Objective:** The loss function requires the model to simultaneously reconstruct two targets in masked autoencoding process: the time-domain reference features to maintain signal fidelity and the frequency-domain features to reflect rhythmic structures. This dual-domain supervised paradigm forces the model to learn universal principles of distinct patterns, thereby achieving highly generalized representation abilities.

We pre-trained Uni-NTFM on a massive corpus containing 28,000 hours of EEG recordings using our specifically designed dual-domain reconstruction self-supervised objective. Extensive experiments on downstream tasks robustly demonstrate the superiority of our new paradigm. Under a linear probing setting without any fine-tuning, the model already exhibits powerful general-purpose representation capabilities. After fine-tuned, Uni-NTFM’s performance on public datasets across more than nine different BCI tasks not only comprehensively surpasses existing task-specific models but also significantly outperforms other mainstream foundation models.

2 METHODOLOGY

This section explains the core paradigm of the Uni-NTFM, a self-supervised foundation model we proposed to address the challenges of large scale EEG representation learning. We think it is necessary to cooperatively analyze three fundamental properties of EEG signals: temporal dynamics, spectral rhythms, and spatial topology. In addition, to efficiently process these complex multi-domain representations, a sparsely-activated MoE pipeline is required. To this end, we have designed a hierarchical information processing paradigm, as shown in Figure 2, which simulates a process of EEG signals from multi-domain perception and cross-domain fusion to high-level cognitive learning.

2.1 INPUT DATA PREPROCESSING

The raw EEG data is processed into tensor shapes of $X \in \mathbb{R}^{B \times R \times E \times T}$, where B is the batch size, R and E are the number of predefined brain regions and the maximum number of electrodes per region, respectively, and T is the length of the time series. To enhance the model’s robustness to common variations in real-world signals, we also simulate noise, channel loss, and temporal drift in signal acquisition through a series of probabilistic data augmentations ($f_{\text{aug}} : X \rightarrow X_{\text{aug}}$) before being entered into the model.

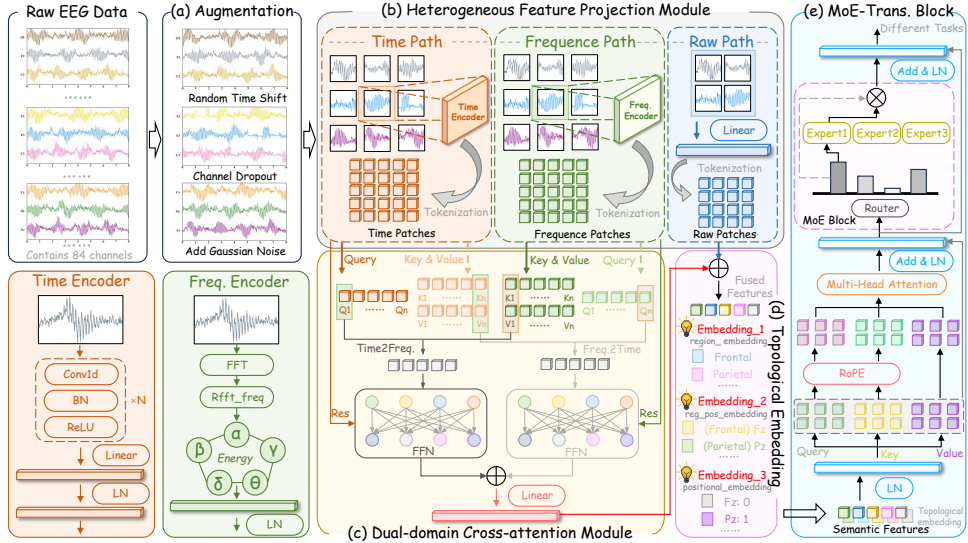


Figure 2: The end-to-end architecture of Uni-NTFM in detail. The data processing flow begins with the data augmentation of raw EEG signals, followed by Heterogeneous Feature Projection Module (HFPN) which parallelly decomposes the input EEG signals into three domain streams: time, frequency, and raw. Next, Dual-domain Cross-attention Module (DCM) performs cross fusion of time domain and frequency domain features, combined with Topological Embedding (TE) to encode the spatial prior information of the electrodes. Finally, the processed representations are sent to the core MoE-Trans. Block to learn universal semantic features.

2.2 DECOUPLING AND SYNERGY OF HETEROGENEOUS FEATURES

Unlike images or text, which have natural discrete units (pixels, words), continuous EEG signals can't be tokenized in this way. A common approach that segments the time series into temporal "patches" ignores the continuous characteristic of the signal and fails to capture features at different temporal scales. To address this, we propose a paradigm: instead of segmenting the time axis, we treat the entire time series $x_i \in \mathbb{R}^T$ (where i is the global electrode index) from each individual electrode as a holistic "patch". Our heterogeneous Feature Projection Module (HFPN) is designed to transform these holistic, channel-wise patches into a set of multi-domain feature embeddings. This module simultaneously projects each channel's signals into three distinct feature domains.

2.2.1 DYNAMICS WAVEFORM ENCODER (TIME PATH)

To capture the local waveform structures and non-stationary events of the signal, we employ a one-dimensional convolutional encoder, $\Phi_T(\cdot)$, to map x_i into a temporal feature vector $h_{i,T} \in \mathbb{R}^D$:

$$h_{i,T} = \Phi_T(x_i) \quad (1)$$

This encoder consists of multiple convolutional blocks, where the operation of each block can be formalized as:

$$h^{(l+1)} = \text{ReLU}(\text{BN}(W^{(l)} * h^{(l)} + b^{(l)})) \quad (2)$$

2.2.2 FREQUENCY DECOMPOSITION ENCODER (FREQUENCY PATH)

To extract the crucial steady-state rhythmic information from the signal, we first decompose the signal into the frequency domain via the Discrete Fourier Transform to compute the Power Spectral Density. Then parameterize it into a mean power vector $P_b \in \mathbb{R}^{N_b}$ for N_b core frequency bands. This vector is subsequently projected into a frequency feature vector $h_{i,F} \in \mathbb{R}^D$ by an MLP, $\Phi_F(\cdot)$.

$$h_{i,F} = \Phi_F(P_b(x_i)) \quad (3)$$

The mean power P_{b_j} for the j -th frequency band is defined as:

$$P_{b_j} = \frac{1}{|\mathcal{K}_j|} \sum_{k \in \mathcal{K}_j} \left| \sum_{t=0}^{T-1} x_i(t) e^{-j2\pi kt/T} \right|^2 \quad (4)$$

where \mathcal{K}_j is the set of discrete frequency indices corresponding to the j -th frequency band.

2.2.3 STANDARD PROJECTION ENCODER (RAW PATH)

While the time and frequency paths perform non-linear transformations that selectively amplify partial features, the raw path establishes a high-quality and information-lossless reference for the self-supervised reconstruction task. This reference representation serves as the “ground truth” target H_R in our reconstruction loss (Section 2.5), ensuring that the model is trained to recover the full signal, not just a specific domain. This design is critical for maintaining the clarity and integrity of the pre-training objective. The explanation for this process is shown in Appendix D.1

2.2.4 DUAL-DOMAIN CROSS-ATTENTION MODULE

Decomposing the signal into parallel temporal and frequency representations, the next critical step is to achieve a unified understanding by modeling their interdependencies. To this end, we introduce the Dual-domain Cross-attention Module (DCM). Distinct from standard self-attention where Query, Key, and Value are from the same source, our module forces a cross-domain dialogue: the temporal feature sequence H_T serves as the Query to probe for relevant Key and Value of frequency features H_F , and vice versa.

$$H'_T = \text{LayerNorm}(H_T + \text{CrossAttn}(Q = H_T, K = H_F, V = H_F)) \quad (5)$$

$$H'_F = \text{LayerNorm}(H_F + \text{CrossAttn}(Q = H_F, K = H_T, V = H_T)) \quad (6)$$

The final fused feature $H_{\text{fused}} = \text{FFN}(\text{Concat}(H'_T, H'_F))$ contains deep interaction information between the two domains.

2.3 EXPLICIT AND UNIFICATION EMBEDDING OF SPATIAL TOPOLOGY

A core limitation of the standard Transformer architecture is its permutation invariance, which makes it inherently unaware of the fixed spatial topology of EEG electrodes. To address this, we introduce the explicit Topological Embedding (TE) that injects this crucial spatial prior directly into the input features.

$$H_{\text{in}} = H_{\text{fused}} + H_R + \mathbf{E}_{\text{region}}[I_{\text{region}}] + \mathbf{E}_{\text{intra}}[I_{\text{intra}}] + \mathbf{E}_{\text{abs}}[I_{\text{abs}}] \quad (7)$$

Our strategy involves creating three distinct types of learnable embeddings whose indices are deterministically generated based on a standard neuroanatomical brain template. These embeddings are: 1) a Region Embedding (E_{region}) that identifies which major brain region an electrode belongs to; 2) an Intra-Region Embedding (E_{intra}) that specifies the electrode’s relative position within that region; and 3) an Absolute Embedding (E_{abs}) that provides a unique identifier for each electrode across the entire array. These three topological embeddings are then wisely added to the signal’s feature representation, as shown in the equation and detailed in Appendix D.2. This process makes the model with a hierarchical and absolute sense of “address” for each electrode, forcing it to learn representations that are necessary of the basic brain topology.

2.4 FUNCTIONALLY MOE-BASED NEURAL TRANSFORMER

The challenge in scaling the Transformer block is that increasing capacity via dense FFN leads to a quadratic increase in computational cost. To overcome this, we replace the dense FFN in each Transformer block with a sparsely-activated MoE mechanism. This architecture is particularly suitable for EEG modeling, as it allows the model to learn specialized subnetworks for distinct signal patterns (e.g., specific neural rhythms, artifacts, or pathological events) through its gating mechanism. This functional specialization not only enhances modeling accuracy but also offers significant advantages in downstream adaptation, where fine-tuning a small subset of relevant experts can lead to highly efficient and robust transfer learning.

$$H'_l = H_{l-1} + \text{MultiHeadSelfAttn}(\text{LayerNorm}(H_{l-1})) \quad (8)$$

$$H_l = H'_l + \text{MoE}(\text{LayerNorm}(H'_l)) \quad (9)$$

2.4.1 NEURAL MULTI-HEAD SELF-ATTENTION

The self-attention mechanism is designed to learn long-range functional connections in the brain. To enable it to perceive the relative spatial order of electrodes, we introduce Rotary Position Encoding (RoPE). For a d -dimensional vector x_m at position m , its rotated form x'_m is obtained by grouping the vector into pairs $(x_{m,2i-1}, x_{m,2i})$ and applying a rotation matrix $\mathbf{R}_{\Theta,m,i}$:

$$\begin{pmatrix} x'_{m,2i-1} \\ x'_{m,2i} \end{pmatrix} = \begin{pmatrix} \cos(m\theta_i) & -\sin(m\theta_i) \\ \sin(m\theta_i) & \cos(m\theta_i) \end{pmatrix} \begin{pmatrix} x_{m,2i-1} \\ x_{m,2i} \end{pmatrix} \quad (10)$$

where $\theta_i = 10000^{-2i/d}$. A property of RoPE is that the attention score intrinsically depends only on the relative position $m - n$:

$$\langle q'_m, k'_n \rangle = \langle \mathbf{R}_{\Theta,m} q_m, \mathbf{R}_{\Theta,n} k_n \rangle = \langle q_m, \mathbf{R}_{\Theta,n-m} k_n \rangle \quad (11)$$

2.4.2 SPARSELY-ACTIVATED MOE MODULE

MoE allows the model to learn function-specific subnetworks. A gating network $g(h_i) = h_i W_g$ computes logits for each input token h_i across N_e expert networks. Through Top-k gating, the final output for a token is the weighted sum of the outputs from the k expert networks $E_j(\cdot)$:

$$\text{MoE}(h_i) = \sum_{j \in \text{TopK}(\text{Softmax}(g(h_i)))} p_j E_j(h_i) \quad (12)$$

To encourage load balancing, we introduce an auxiliary loss \mathcal{L}_{aux} :

$$\mathcal{L}_{\text{aux}} = \alpha \cdot N_e \sum_{j=1}^{N_e} f_j \cdot \bar{p}_j \quad (13)$$

where f_j is the fraction of tokens routed to expert j , and \bar{p}_j is the average probability assigned to expert j for those tokens.

2.5 DUAL-DOMAIN SELF-SUPERVISED RECONSTRUCTION OBJECTIVE

The entire learning process is driven by the masked autoencoding self-supervised task (He et al., 2022). For an input sequence H_{in} , we randomly select an index subset \mathcal{M} and replace its tokens with a shared, learnable embedding $e_{[\text{MASK}]}$. The model’s optimization objective is to reconstruct the original features of the masked tokens. To this end, we designed a Dual-Domain Loss Function, $\mathcal{L}_{\text{total}}$, which forces the model to maintain consistency in both the time and frequency domains simultaneously:

$$\mathcal{L}_{\text{total}} = \lambda_T \mathcal{L}_{\text{time}} + \lambda_F \mathcal{L}_{\text{freq}} + \lambda_{\text{aux}} \mathcal{L}_{\text{aux}} \quad (14)$$

The temporal reconstruction loss $\mathcal{L}_{\text{time}}$ and frequency reconstruction loss $\mathcal{L}_{\text{freq}}$ are calculated as the Mean Squared Error over the masked positions \mathcal{M} :

$$\mathcal{L}_{\text{time}} = \frac{1}{|\mathcal{M}|} \sum_{i \in \mathcal{M}} \|\text{Head}_T(H_{\text{out},i}) - h_{i,R}\|_2^2 \quad (15)$$

$$\mathcal{L}_{\text{freq}} = \frac{1}{|\mathcal{M}|} \sum_{i \in \mathcal{M}} \|\text{Head}_F(H_{\text{out},i}) - h_{i,F}\|_2^2 \quad (16)$$

where H_{out} is the final output of the Transformer. This learning paradigm enables Uni-NTFM to learn the profound internal structures and regularities of EEG signals without explicit labels.

3 EXPERIMENTS

3.1 PRE-TRAINING SETTINGS

1) Data Summary. We aggregated a large-scale pre-training corpus by amalgamating nine distinct, publicly available EEG datasets to train a foundation model capable of learning truly generalizable neural representations. As detailed in Appendix Table 6, this corpus comprises data from

over 17,000 subjects and amounts to approximately 28,000 hours of recordings. It includes recordings from resting-state conditions (e.g., REEG-BACA (Getzmann et al., 2024), Resting State EEG (Trujillo et al., 2017)), emotion induction tasks (e.g., Emobrain (Savran¹ et al., 2006), SEED-series (Zheng et al., 2018; Liu et al., 2021; 2022)), cognitive classification tasks (e.g., Raw EEG Data (Trujillo, 2020)), BCI paradigms (BCI Competition IV-1 (Blankertz et al., 2007)), and extensive clinical recordings from hospital environments (e.g., TUEG (Obeid & Picone, 2016), CAUEEG (Kim et al., 2023), Siena Scalp EEG Database (Detti et al., 2020)).

2) Data Preprocessing. Initially, a zero-phase filter was applied with a passband of 0.5-50 Hz, and a notch filter suppressed powerline interference at 50 Hz and its harmonics. To ensure a uniform temporal resolution, all signals were then downsampled to a consistent 200 Hz sampling rate. Before normalization, all channel amplitudes were uniformly scaled to millivolts (mV).

3) Training Settings. We designed four versions of Uni-NTFM at different scales, with 57M, 427M, 912M, and 1.9B parameters, respectively. All experiments were conducted on NVIDIA A100-80G GPUs, using Python 3.9.23 and PyTorch 2.3.1 with CUDA 11.8. The specific configurations for each model and other detailed hyperparameter settings are provided in Appendix Table 8.

3.2 DOWNSTREAM DATASETS

1) Data Summary. To comprehensively evaluate the performance of Uni-NTFM, we collected nine public EEG datasets across various paradigms and tasks, as detailed in Appendix Table 7: 1) TUAB (Harati et al., 2015), 2) TUEV (Harati et al., 2015), 3) SEED (Zheng & Lu, 2015), 4) TDBrain (Van Dijk et al., 2022), 5) ADFTD (Miltiadous et al., 2023), 6) BCIC-IV-2a (Brunner et al., 2008), 7) Workload (Zyma et al., 2019), 8) HMC (Alvarez-Estevez & Rijssman, 2021), and 9) TUSL (von Weltin et al., 2017). We employed two evaluation strategies: first, we used linear probing to directly evaluate the quality of the representations learned by the pre-trained model; second, we conducted full fine-tuning on downstream tasks to check the model’s generalization and adaptation abilities.

2) Evaluation Metrics. We choose the following metrics to evaluate the model’s generalization abilities across various tasks: **A) Balanced Accuracy:** The metric is defined as the arithmetic mean of each class’s recall. **B) AUROC:** The metric represents the model’s ability to distinguish between classes, which is independent of the chosen classification threshold. **C) AUC-PR:** The metric is the area under the curve that plots precision against recall for different classification thresholds. **D) Cohen’s Kappa (κ):** The metric is used to measure the agreement between a classifier’s predictions and the ground truth. **E) F1-Score:** The metric is the harmonic mean of precision and recall. In the subsequent experiments, we select Balanced Accuracy, AUROC, and AUC-PR as the evaluation metric for binary classification tasks. And we adopt Balanced Accuracy, Cohen’s Kappa, and F1-Score to evaluate the performance on multi-class classification tasks. The detailed introduction of the formulas is in Appendix C.

3.3 RESULTS ON DOWNSTREAM DATASETS

To comprehensively evaluate the generalization abilities of Uni-NTFM, we assessed its performance across nine diverse downstream tasks using two distinct strategies: linear probing of the frozen pre-trained model and full fine-tuning. As detailed in Table 1, 2, 3, our results consistently demonstrate the superiority of the Uni-NTFM paradigm, establishing a new state-of-the-art (SOTA) across a wide field of EEG analysis application. In addition, we also conducted scaling law experiments on Uni-NTFM, and the detailed results can be found in Appendix G.

1) Linear Probing Performance:

Under the linear probing setting, which directly measures the intrinsic quality of the learned representations, Uni-NTFM exhibits remarkable zero-shot transfer abilities. Even without fine-tuning, the model consistently outperforms traditional task-specific methods and other pretrained foundation models across the majority of tasks. Specifically, on the TUAB abnormal detection task, the Uni-NTFM_{large} model achieves a Balanced Accuracy of 0.7844, significantly surpassing the task-specific SPARCNet model. This performance across varied tasks, from clinical event detection to cognitive state classification, highlights the universal representations learned through our proposed dual-domain, structure-aware pretraining objective.

Table 1: Best performances on TUAB, TUEV, and SEED.

Method	TUAB (2-class)			TUEV (6-class)			SEED (3-class)		
	Balanced Acc.	AUC-PR	AUROC	Balanced Acc.	Cohen's Kappa	Weighted F1	Balanced Acc.	Cohen's Kappa	Weighted F1
<i>Traditional Task-specific Methods (Single-task)</i>									
SPaRCNet (Jing et al., 2023)	0.7749 \pm 0.0091	0.8314 \pm 0.0071	0.8631 \pm 0.0058	0.4315 \pm 0.0317	0.4379 \pm 0.0217	0.6814 \pm 0.0167	0.5736 \pm 0.0292	0.3527 \pm 0.0412	0.5635 \pm 0.0223
EEGNet (?)	0.7712 \pm 0.0056	0.8231 \pm 0.0029	0.8501 \pm 0.0027	0.3975 \pm 0.0107	0.3493 \pm 0.0113	0.6384 \pm 0.0206	0.6249 \pm 0.0352	0.4473 \pm 0.0229	0.6177 \pm 0.0266
CNN-Transformer (Peh et al., 2022)	0.7824 \pm 0.0107	0.8486 \pm 0.0098	0.8488 \pm 0.0076	0.4194 \pm 0.0128	0.3932 \pm 0.0172	0.6782 \pm 0.0217	0.6161 \pm 0.0381	0.4262 \pm 0.0601	0.6150 \pm 0.0463
EEGConformer (Song et al., 2022)	0.7746 \pm 0.0037	0.8431 \pm 0.0065	0.8503 \pm 0.0054	0.4134 \pm 0.0261	0.4027 \pm 0.0181	0.6972 \pm 0.0149	0.6742 \pm 0.0207	0.4618 \pm 0.0199	0.6431 \pm 0.0529
FFCL (Li et al., 2022)	0.7794 \pm 0.0019	0.8433 \pm 0.0038	0.8594 \pm 0.0066	0.4002 \pm 0.0155	0.3697 \pm 0.0211	0.6799 \pm 0.0137	0.5776 \pm 0.0261	0.3768 \pm 0.0328	0.5813 \pm 0.0233
ST-Transformer (Song et al., 2021)	0.7928 \pm 0.0017	0.8536 \pm 0.0057	0.8689 \pm 0.0024	0.3833 \pm 0.0228	0.6911 \pm 0.0177	0.5639 \pm 0.0177	0.3744 \pm 0.0182	0.5627 \pm 0.0144	
ContraWR (Yang et al., 2023b)	0.7752 \pm 0.0044	0.8460 \pm 0.0068	0.8461 \pm 0.0067	0.4358 \pm 0.0271	0.3988 \pm 0.0168	0.6836 \pm 0.0145	0.6034 \pm 0.0066	0.4131 \pm 0.0132	0.6099 \pm 0.0113
<i>Only Pretrained Foundation Models (Multi-tasks)</i>									
NeuroLM-XL (Jiang et al., 2024a)	0.7969 \pm 0.0091	0.7219 \pm 0.0082	0.7884 \pm 0.0194	0.4679 \pm 0.0356	0.4570 \pm 0.0498	0.7359 \pm 0.0219	0.6034 \pm 0.0110	0.4082 \pm 0.0036	0.6063 \pm 0.0030
EEGPT (Wang et al., 2024a)	0.7922 \pm 0.0046	0.7455 \pm 0.0059	0.8662 \pm 0.0079	0.6232 \pm 0.0114	0.6351 \pm 0.0134	0.8187 \pm 0.0063	0.7122 \pm 0.0022	0.5734 \pm 0.0049	0.7099 \pm 0.0038
<i>Uni</i> – <i>NTFM</i> _{tiny}	0.7136 \pm 0.0218	0.7707 \pm 0.0159	0.7821 \pm 0.0142	0.5694 \pm 0.0198	0.6011 \pm 0.0172	0.7691 \pm 0.0191	0.6746 \pm 0.0048	0.5511 \pm 0.0072	0.6871 \pm 0.0055
<i>Uni</i> – <i>NTFM</i> _{small}	0.7450 \pm 0.0125	0.7931 \pm 0.0172	0.8056 \pm 0.0114	0.5933 \pm 0.0161	0.6312 \pm 0.0208	0.7915 \pm 0.0258	0.6886 \pm 0.0093	0.5623 \pm 0.0049	0.6992 \pm 0.0047
<i>Uni</i> – <i>NTFM</i> _{middle}	0.7671 \pm 0.0133	0.8144 \pm 0.0155	0.8182 \pm 0.0112	0.6101 \pm 0.0137	0.6479 \pm 0.0122	0.8137 \pm 0.0160	0.6951 \pm 0.0087	0.5717 \pm 0.0059	0.7076 \pm 0.0055
<i>Uni</i> – <i>NTFM</i> _{large}	0.7844 \pm 0.0096	0.8259 \pm 0.0171	0.8278 \pm 0.0136	0.6244 \pm 0.0199	0.6548 \pm 0.0142	0.8213 \pm 0.0139	0.7025 \pm 0.0064	0.5781 \pm 0.0066	0.7142 \pm 0.0039
<i>Pretrained and Fine-tuned Foundation Models (Single-task)</i>									
BIOT (Yang et al., 2023a)	0.7959 \pm 0.0057	0.8792 \pm 0.0023	0.8815 \pm 0.0043	0.5281 \pm 0.0225	0.5273 \pm 0.0249	0.7492 \pm 0.0082	0.7097 \pm 0.0024	0.5682 \pm 0.0051	0.7134 \pm 0.0027
LaBraM-Base (Jiang et al., 2024b)	0.8140 \pm 0.0019	0.8965 \pm 0.0016	0.9022 \pm 0.0009	0.6409 \pm 0.0065	0.6637 \pm 0.0093	0.8312 \pm 0.0052	0.7318 \pm 0.0019	0.5994 \pm 0.0031	0.7354 \pm 0.0021
CBraMod (Wang et al., 2024b)	0.7891 \pm 0.0030	0.8636 \pm 0.0063	0.8606 \pm 0.0057	0.6671 \pm 0.0107	0.6772 \pm 0.0096	0.8342 \pm 0.0064	0.7272 \pm 0.0066	0.5764 \pm 0.0017	0.7301 \pm 0.0041
CSBrain * (Zhou et al., 2025b)	0.8172 \pm 0.0043	0.9005 \pm 0.0066	0.8957 \pm 0.0046	0.6903 \pm 0.0059	0.6833 \pm 0.0047	0.8333 \pm 0.0057	0.7302 \pm 0.0038	0.5931 \pm 0.0026	0.7298 \pm 0.0036
<i>Uni</i> – <i>NTFM</i> _{tiny}	0.7649 \pm 0.0131	0.8230 \pm 0.0152	0.8325 \pm 0.0126	0.6405 \pm 0.0142	0.6582 \pm 0.0145	0.7118 \pm 0.0097	0.7118 \pm 0.0054	0.5762 \pm 0.0118	0.7197 \pm 0.0023
<i>Uni</i> – <i>NTFM</i> _{small}	0.7893 \pm 0.0062	0.8553 \pm 0.0141	0.8601 \pm 0.0087	0.6694 \pm 0.0108	0.6796 \pm 0.0110	0.8325 \pm 0.0137	0.7202 \pm 0.0033	0.5859 \pm 0.0065	0.7274 \pm 0.0049
<i>Uni</i> – <i>NTFM</i> _{middle}	0.8081 \pm 0.0088	0.8795 \pm 0.0091	0.8837 \pm 0.0066	0.6886 \pm 0.0157	0.6922 \pm 0.0133	0.8409 \pm 0.0083	0.7290 \pm 0.0051	0.5922 \pm 0.0082	0.7342 \pm 0.0044
<i>Uni</i> – <i>NTFM</i> _{large}	0.8197 \pm 0.0040	0.8982 \pm 0.0058	0.8964 \pm 0.0118	0.6991 \pm 0.0170	0.7030 \pm 0.0148	0.8460 \pm 0.0132	0.7337 \pm 0.0045	0.5976 \pm 0.0058	0.7381 \pm 0.0069

* The CSBrain code is not open-source, and the data in the table is all provided from its paper.

Table 2: Best performances on TDBrain, ADFTD, and BCIC-IV-2a.

Method	TDBrain (2-class)			ADFTD (3-class)			BCIC-IV-2a (4-class)		
	Balanced Acc.	AUC-PR	AUROC	Balanced Acc.	Cohen's Kappa	Weighted F1	Balanced Acc.	Cohen's Kappa	Weighted F1
<i>Traditional Task-specific Methods (Single-task)</i>									
SPaRCNet (Jing et al., 2023)	0.7467 \pm 0.0106	0.8266 \pm 0.0092	0.8179 \pm 0.0116	0.7132 \pm 0.0156	0.7288 \pm 0.0212	0.7337 \pm 0.0119	0.4697 \pm 0.0141	0.2871 \pm 0.0129	0.4460 \pm 0.0137
EEGNet (Lawhern et al., 2018)	0.7516 \pm 0.0135	0.8273 \pm 0.0088	0.8314 \pm 0.0195	0.7432 \pm 0.0159	0.7666 \pm 0.0199	0.7442 \pm 0.0167	0.4462 \pm 0.0113	0.2647 \pm 0.0109	0.4302 \pm 0.0124
CNN-Transformer (Peh et al., 2022)	0.7813 \pm 0.0027	0.8294 \pm 0.0023	0.8462 \pm 0.0087	0.7091 \pm 0.0226	0.6729 \pm 0.0255	0.4583 \pm 0.0161	0.2825 \pm 0.0139	0.4473 \pm 0.0128	
EEGConformer (Song et al., 2022)	0.7925 \pm 0.0319	0.8381 \pm 0.0161	0.8531 \pm 0.0201	0.7388 \pm 0.0123	0.7339 \pm 0.0111	0.7301 \pm 0.0159	0.4677 \pm 0.0148	0.2917 \pm 0.0175	0.4582 \pm 0.0139
FFCL (Li et al., 2022)	0.7899 \pm 0.0210	0.8156 \pm 0.0219	0.8415 \pm 0.0081	0.7062 \pm 0.0131	0.6825 \pm 0.0236	0.7060 \pm 0.0214	0.4511 \pm 0.0105	0.2714 \pm 0.0189	0.4323 \pm 0.0170
ST-Transformer (Song et al., 2021)	0.7737 \pm 0.0102	0.8339 \pm 0.0096	0.8336 \pm 0.0132	0.7504 \pm 0.0156	0.7344 \pm 0.0231	0.7482 \pm 0.0266	0.4521 \pm 0.0166	0.2709 \pm 0.0155	0.4463 \pm 0.0192
ContraWR (Yang et al., 2023b)	0.8017 \pm 0.0179	0.8422 \pm 0.0154	0.8604 \pm 0.0177	0.7211 \pm 0.0110	0.7522 \pm 0.0299	0.7375 \pm 0.0279	0.4682 \pm 0.0137	0.2894 \pm 0.0141	0.4434 \pm 0.0153
<i>Only Pretrained Foundation Models (Multi-tasks)</i>									
NeuroLM-XL (Jiang et al., 2024a)	0.7629 \pm 0.0132	0.7481 \pm 0.0167	0.7552 \pm 0.0114	0.6746 \pm 0.0164	0.6828 \pm 0.0104	0.7252 \pm 0.0097	0.5195 \pm 0.0074	0.3874 \pm 0.0091	0.4922 \pm 0.0061
EEGPT (Wang et al., 2024a)	0.8194 \pm 0.0162	0.8377 \pm 0.0089	0.8561 \pm 0.0103	0.6531 \pm 0.0127	0.6292 \pm 0.0088	0.6392 \pm 0.0074	0.5281 \pm 0.0055	0.4033 \pm 0.0062	0.5129 \pm 0.0068
<i>Uni</i> – <i>NTFM</i> _{tiny}	0.8166 \pm 0.0052	0.8519 \pm 0.0087	0.8533 \pm 0.0074	0.6661 \pm 0.0088	0.6625 \pm 0.0071	0.7029 \pm 0.0094	0.5122 \pm 0.0073	0.3968 \pm 0.0086	0.5025 \pm 0.0065
<i>Uni</i> – <i>NTFM</i> _{small}	0.8207 \pm 0.0097	0.8562 \pm 0.0117	0.8618 \pm 0.0102	0.6735 \pm 0.0049	0.6744 \pm 0.0113	0.7131 \pm 0.0072	0.5209 \pm 0.0067	0.4044 \pm 0.0102	0.5123 \pm 0.0046
<i>Uni</i> – <i>NTFM</i> _{middle}	0.8212 \pm 0.0061	0.8570 \pm 0.0081	0.8672 \pm 0.0119	0.6780 \pm 0.0077	0.7208 \pm 0.0067	0.7208 \pm 0.0067	0.5266 \pm 0.0036	0.4107 \pm 0.0079	0.5077 \pm 0.0131
<i>Uni</i> – <i>NTFM</i> _{large}	0.8246 \pm 0.0043	0.8584 \pm 0.0136	0.8691 \pm 0.0079	0.6813 \pm 0.0064	0.6822 \pm 0.0135	0.7260 \pm 0.0079	0.5258 \pm 0.0062	0.4118 \pm 0.0145	0.5144 \pm 0.0105
<i>Pretrained and Fine-tuned Foundation Models (Single-task)</i>									
BIOT (Yang et al., 2023a)	0.8066 \pm 0.0073	0.8494 \pm 0.0135	0.8531 \pm 0.0066	0.7763 \pm 0.0091	0.7448 \pm 0.0043	0.7721 \pm 0.0079	0.4748 \pm 0.0093	0.2997 \pm 0.0139	0.4607 \pm 0.0125
LaBraM-Base (Jiang et al., 2024b)	0.8125 \pm 0.0091	0.8422 \pm 0.0047	0.8648 \pm 0.0055	0.7492 \pm 0.0138	0.7747 \pm 0.0083	0.5597 \pm 0.0049	0.4166 \pm 0.0114	0.5623 \pm 0.0045	
CBraMod (Wang et al., 2024b)	0.8281 \pm 0.0064	0.8537 \pm 0.0078	0.8744 \pm 0.0085	0.7369 \pm 0.0112	0.7559 \pm 0.0088	0.7533 \pm 0.0046	0.5138 \pm 0.0066	0.3518 \pm 0.0094	0.4984 \pm 0.0085
CSBrain * (Zhou et al., 2025b)	—	—	—	—	—	—	0.5657 \pm 0.0071	0.4209 \pm 0.0093	0.5637 \pm 0.0087
<i>Uni</i> – <i>NTFM</i> _{tiny}	0.8226 \pm 0.0039	0.8556 \pm 0.0093	0.8611 \pm 0.0078	0.7470 \pm 0.0062	0.7517 \pm 0.0086	0.7616 \pm 0.0051	0.5423 \pm 0.0048	0.4143 \pm 0.0061	0.5411<math

Table 3: Best performances on Workload, HMC, and TUSL.

Method	Workload (2-class)			HMC (5-class)			TUSL (3-class)		
	Balanced Acc.	AUC-PR	AUROC	Balanced Acc.	Cohen's Kappa	Weighted F1	Balanced Acc.	Cohen's Kappa	Weighted F1
<i>Traditional Task-specific Methods (Single-task)</i>									
SPaRCNet (Jing et al., 2023)	0.6132 \pm 0.0047	0.6726 \pm 0.0248	0.6839 \pm 0.0224	0.5537 \pm 0.0374	0.4788 \pm 0.0297	0.5698 \pm 0.0434	0.5685 \pm 0.0251	0.4916 \pm 0.0401	0.5844 \pm 0.0486
EEGNet (Lawhern et al., 2018)	0.6085 \pm 0.0255	0.5817 \pm 0.0201	0.6238 \pm 0.0151	0.6216 \pm 0.0212	0.5614 \pm 0.0188	0.6277 \pm 0.0142	0.5737 \pm 0.0417	0.4983 \pm 0.0448	0.5292 \pm 0.0688
CNN-Transformer (Pehl et al., 2022)	0.5911 \pm 0.0195	0.5723 \pm 0.0337	0.5981 \pm 0.0266	0.6419 \pm 0.0286	0.5822 \pm 0.0266	0.6736 \pm 0.0177	0.5562 \pm 0.0181	0.4872 \pm 0.0206	0.5644 \pm 0.0265
EEGConformer (Song et al., 2022)	0.6587 \pm 0.0219	0.6922 \pm 0.0185	0.6877 \pm 0.0332	0.6978 \pm 0.0144	0.6216 \pm 0.0234	0.6887 \pm 0.0122	0.5972 \pm 0.0812	0.5133 \pm 0.0476	0.6002 \pm 0.0416
FFCL (Li et al., 2022)	0.6728 \pm 0.0341	0.7649 \pm 0.0115	0.7566 \pm 0.0301	0.6368 \pm 0.0363	0.5538 \pm 0.0213	0.6674 \pm 0.0360	0.5876 \pm 0.0191	0.4704 \pm 0.0157	0.5136 \pm 0.0192
ST-Transformer (Song et al., 2021)	0.6043 \pm 0.0125	0.5681 \pm 0.0141	0.6255 \pm 0.0167	0.5949 \pm 0.0543	0.5003 \pm 0.0201	0.6147 \pm 0.0331	0.4928 \pm 0.0557	0.3016 \pm 0.1007	0.4120 \pm 0.0588
ContraWR (Yang et al., 2023b)	0.6755 \pm 0.0242	0.7591 \pm 0.0280	0.7633 \pm 0.0229	0.6159 \pm 0.0623	0.5689 \pm 0.0442	0.6231 \pm 0.0183	0.5833 \pm 0.0391	0.4267 \pm 0.0281	0.5508 \pm 0.0466
<i>Only Pretrained Foundation Models (Multi-tasks)</i>									
NeuroLM-XL (Jiang et al., 2024a)	0.6345 \pm 0.0442	0.5889 \pm 0.0423	0.6130 \pm 0.0764	0.5761 \pm 0.1084	0.4795 \pm 0.1466	0.5883 \pm 0.1286	0.6845 \pm 0.0304	0.5194 \pm 0.0461	0.6839 \pm 0.0297
EEGPT (Wang et al., 2024a)	0.6299 \pm 0.0178	0.6792 \pm 0.0092	0.6928 \pm 0.0108	0.7029 \pm 0.0082	0.6584 \pm 0.0059	0.7323 \pm 0.0041	0.7288 \pm 0.0143	0.5972 \pm 0.0209	0.7233 \pm 0.0153
<i>Uni</i> – <i>NTFM_{tiny}</i>	0.6306 \pm 0.0144	0.6654 \pm 0.0198	0.6955 \pm 0.0187	0.6985 \pm 0.0245	0.6373 \pm 0.0241	0.6934 \pm 0.0071	0.7108 \pm 0.0157	0.6255 \pm 0.0321	0.7138 \pm 0.0251
<i>Uni</i> – <i>NTFM_{small}</i>	0.6411 \pm 0.0229	0.6771 \pm 0.0318	0.7026 \pm 0.0216	0.7088 \pm 0.0238	0.6503 \pm 0.0138	0.7155 \pm 0.0162	0.7229 \pm 0.0090	0.6373 \pm 0.0214	0.7220 \pm 0.0311
<i>Uni</i> – <i>NTFM_{middle}</i>	0.6379 \pm 0.0153	0.6786 \pm 0.0161	0.7099 \pm 0.0134	0.7134 \pm 0.0161	0.6558 \pm 0.0108	0.7176 \pm 0.0092	0.7256 \pm 0.0144	0.6352 \pm 0.0141	0.7255 \pm 0.0266
<i>Uni</i> – <i>NTFM_{large}</i>	0.6416 \pm 0.0268	0.6848 \pm 0.0183	0.7087 \pm 0.0168	0.7155 \pm 0.0233	0.6611 \pm 0.0145	0.7244 \pm 0.0111	0.7314 \pm 0.0115	0.6411 \pm 0.0266	0.7313 \pm 0.0361
<i>Pretrained and Fine-tuned Foundation Models (Single-task)</i>									
BIOT (Yang et al., 2023a)	0.6655 \pm 0.0665	0.7189 \pm 0.0722	0.7342 \pm 0.0536	0.6862 \pm 0.0041	0.6295 \pm 0.0113	0.7091 \pm 0.0147	0.5758 \pm 0.0303	0.2012 \pm 0.0212	0.2394 \pm 0.0040
LaBra-Base (Jiang et al., 2024b)	0.6609 \pm 0.0204	0.7174 \pm 0.0234	0.7272 \pm 0.0165	0.7286 \pm 0.0101	0.6812 \pm 0.0073	0.7554 \pm 0.0024	0.7625 \pm 0.0131	0.6407 \pm 0.0304	0.7614 \pm 0.0210
CBraMod (Wang et al., 2024b)	0.6537 \pm 0.0260	0.7039 \pm 0.0133	0.7007 \pm 0.0232	0.7269 \pm 0.0041	0.6683 \pm 0.0103	0.7395 \pm 0.0089	0.7388 \pm 0.0320	0.6149 \pm 0.0550	0.7453 \pm 0.0360
CSBrain *	(Zhou et al., 2025b)	—	—	0.7345 \pm 0.0047	0.6818 \pm 0.0046	0.7506 \pm 0.0042	0.8571 \pm 0.0240	0.7828 \pm 0.0270	0.8568 \pm 0.0180
<i>Uni</i> – <i>NTFM_{tiny}</i>	0.6560 \pm 0.0225	0.7084 \pm 0.0219	0.7262 \pm 0.0129	0.7244 \pm 0.0199	0.6691 \pm 0.0122	0.7443 \pm 0.0078	0.7669 \pm 0.0236	0.6621 \pm 0.0211	0.7645 \pm 0.0207
<i>Uni</i> – <i>NTFM_{small}</i>	0.6672 \pm 0.0171	0.7173 \pm 0.0159	0.7388 \pm 0.0150	0.7237 \pm 0.0186	0.6769 \pm 0.0134	0.7551 \pm 0.0069	0.7800 \pm 0.0271	0.6752 \pm 0.0133	0.7710 \pm 0.0133
<i>Uni</i> – <i>NTFM_{middle}</i>	0.6616 \pm 0.0224	0.7166 \pm 0.0113	0.7346 \pm 0.0172	0.7288 \pm 0.0100	0.6777 \pm 0.0115	0.7512 \pm 0.0120	0.7779 \pm 0.0306	0.6775 \pm 0.0314	0.7691 \pm 0.0262
<i>Uni</i> – <i>NTFM_{large}</i>	0.6644 \pm 0.0147	0.7228 \pm 0.0132	0.7492 \pm 0.0101	0.7311 \pm 0.0097	0.6832 \pm 0.0077	0.7572 \pm 0.0054	0.7844 \pm 0.0255	0.6853 \pm 0.0130	0.7746 \pm 0.0145

* The CSBrain code is not open-source, and the table in the paper is all provided from its paper.

Table 4: Ablation study on TUAB dataset.

Dataset	Number	HFPFM	DCM	TE	MoE	Balanced Acc.	AUC-PR	AUROC
TUAB (2-class)	A1	✗	✗	✗	✗	0.6252 \pm 0.0483	0.6871 \pm 0.0369	0.7116 \pm 0.0537
	A2	✓	✗	✗	✗	0.6995 \pm 0.0324	0.7778 \pm 0.0290	0.7805 \pm 0.0253
	A3	✓	✓	✗	✗	0.7364 \pm 0.0231	0.7992 \pm 0.0211	0.7976 \pm 0.0285
	A4	✗	✗	✓	✗	0.6740 \pm 0.0361	0.7405 \pm 0.0288	0.7614 \pm 0.0339
	A5	✗	✗	✗	✓	0.6623 \pm 0.0208	0.7387 \pm 0.0244	0.7862 \pm 0.0251
	A6	✗	✗	✓	✓	0.7181 \pm 0.0195	0.7849 \pm 0.0146	0.8003 \pm 0.0212
	A7	✓	✗	✓	✓	0.7334 \pm 0.0242	0.7933 \pm 0.0186	0.8110 \pm 0.0255
	A8	✓	✓	✗	✓	0.7496 \pm 0.0192	0.8137 \pm 0.0164	0.8239 \pm 0.0205
	A9	✓	✓	✓	✗	0.7417 \pm 0.0163	0.8094 \pm 0.0228	0.8140 \pm 0.0190
	A10	✓	✓	✓	✓	0.7649 \pm 0.0131	0.8230 \pm 0.0152	0.8325 \pm 0.0126

HFPFM: Heterogeneous Feature Projection Module; DCM: Dual-domain Cross-attention Module; TE: Topological Embedding; and MoE: Mixture-of-Experts.

Table 5: Ablation study on TUEV dataset.

Dataset	Number	HFPFM	DCM	TE	MoE	Balanced Acc.	Cohen's Kappa	Weighted F1
TUEV (6-class)	B1	✗	✗	✗	✗	0.5874 \pm 0.0316	0.6229 \pm 0.0227	0.7366 \pm 0.0282
	B2	✓	✗	✗	✗	0.6145 \pm 0.0256	0.6334 \pm 0.0258	0.7669 \pm 0.0351
	B3	✓	✓	✗	✗	0.6288 \pm 0.0195	0.6393 \pm 0.0215	0.7872 \pm 0.0167
	B4	✗	✗	✓	✗	0.6060 \pm 0.0254	0.6411 \pm 0.0199	0.7781 \pm 0.0171
	B5	✗	✗	✗	✓	0.5986 \pm 0.0344	0.6279 \pm 0.0265	0.7552 \pm 0.0213
	B6	✗	✗	✓	✓	0.6150 \pm 0.0202	0.6428 \pm 0.0237	0.7894 \pm 0.0223
	B7	✓	✗	✓	✓	0.6335 \pm 0.0249	0.6539 \pm 0.0188	0.8081 \pm 0.0241
	B8	✓	✓	✗	✓	0.6316 \pm 0.0173	0.6480 \pm 0.0189	0.8019 \pm 0.0116
	B9	✓	✓	✓	✗	0.6353 \pm 0.0220	0.6441 \pm 0.0175	0.7939 \pm 0.0142
	B10	✓	✓	✓	✓	0.6405 \pm 0.0142	0.6582 \pm 0.0145	0.8174 \pm 0.0097

HFPFM: Heterogeneous Feature Projection Module; DCM: Dual-domain Cross-attention Module; TE: Topological Embedding; and MoE: Mixture-of-Experts.

4 CONCLUSIONS

This paper introduces the Unified Neural Topological Foundation Model (Uni-NTFM), which counters the limitations of traditional models by adopting an architecture designed from the first principles of neuroscience. Specifically, we simultaneously process the temporal, frequency, and standard properties of EEG signals, and insert the spatial priors of multi-domain representations before transfer into the scalable MoE neural Transformer for specialized feature processing. Moreover, pretrained on over 28,000 hours of data, Uni-NTFM sets the standard across nine downstream tasks, demonstrating superior generalization. The success of our model validates the structure-aware modeling theory that respects the characteristics of neural signals is necessary for releasing the potential of large-scale brain foundation models. We hope this work provides a method for the next generation of efficient and interpretable brain-intelligence interfaces in neuroscience applications.

ETHICS STATEMENT

This research was conducted exclusively using publicly available and fully anonymized EEG datasets. Our model, Uni-NTFM, is intended for foundational research purposes. We acknowledge that potential biases may be inherited from the training data, and addressing fairness is a critical step for future real-world applications. The overarching goal of this work is to contribute positively to the fields of neuroscience and medicine.

REPRODUCIBILITY

To ensure full reproducibility, we will provide the following:

- **Code and Models:** All source code will be released under an open-source license at <https://anonymous.4open.science/r/Uni-NTFM-0924>.
- **Datasets:** All datasets for pre-training and evaluation are publicly available and are detailed in Appendix Table 6 and Table 7, respectively.
- **Hyperparameters:** Detailed configurations and hyperparameters for all model variants and experiments are provided in the Appendix (Table 8, 9, 10, 11).
- **Environment:** The computing environment is specified in Section 3.1.

REFERENCES

- Josh Achiam, Steven Adler, Sandhini Agarwal, Lama Ahmad, Ilge Akkaya, Florencia Leoni Aleman, Diogo Almeida, Janko Altenschmidt, Sam Altman, Shyamal Anadkat, et al. Gpt-4 technical report. *arXiv preprint arXiv:2303.08774*, 2023.
- Diego Alvarez-Estevez and Roselyne M Rijsman. Inter-database validation of a deep learning approach for automatic sleep scoring. *PloS one*, 16(8):e0256111, 2021.
- Bruno Aristimunha, Dung Truong, Pierre Guetschel, Seyed Yahya Shirazi, Isabelle Guyon, Alexandre R Franco, Michael P Milham, Aviv Dotan, Scott Makeig, Alexandre Gramfort, et al. Eeg foundation challenge: From cross-task to cross-subject eeg decoding. *arXiv preprint arXiv:2506.19141*, 2025.
- Naseem Babu, Jimson Mathew, and AP Vinod. Large language models for eeg: A comprehensive survey and taxonomy. *arXiv preprint arXiv:2506.06353*, 2025.
- Hubert Banville, Omar Chehab, Aapo Hyvärinen, Denis-Alexander Engemann, and Alexandre Gramfort. Uncovering the structure of clinical eeg signals with self-supervised learning. *Journal of Neural Engineering*, 18(4):046020, 2021.
- Benjamin Blankertz, Guido Dornhege, Matthias Krauledat, Klaus-Robert Müller, and Gabriel Curio. The non-invasive berlin brain–computer interface: fast acquisition of effective performance in untrained subjects. *NeuroImage*, 37(2):539–550, 2007.
- Clemens Brunner, Robert Leeb, Gernot Müller-Putz, Alois Schlögl, and Gert Pfurtscheller. Bci competition 2008–graz data set a. *Institute for knowledge discovery (laboratory of brain-computer interfaces), Graz University of Technology*, 16(1-6):34, 2008.
- Paolo Detti, Giampaolo Vatti, and Garazi Zabalo Manrique de Lara. Eeg synchronization analysis for seizure prediction: A study on data of noninvasive recordings. *Processes*, 8(7):846, 2020.
- Jacob Devlin, Ming-Wei Chang, Kenton Lee, and Kristina Toutanova. Bert: Pre-training of deep bidirectional transformers for language understanding. In *Proceedings of the 2019 conference of the North American chapter of the association for computational linguistics: human language technologies, volume 1 (long and short papers)*, pp. 4171–4186, 2019.
- Sharlene N Flesher, John E Downey, Jeffrey M Weiss, Christopher L Hughes, Angelica J Herrera, Elizabeth C Tyler-Kabara, Michael L Boninger, Jennifer L Collinger, and Robert A Gaunt. A brain-computer interface that evokes tactile sensations improves robotic arm control. *Science*, 372(6544):831–836, 2021.

Stephan Getzmann, Patrick D Gajewski, Daniel Schneider, and Edmund Wascher. Resting-state eeg data before and after cognitive activity across the adult lifespan and a 5-year follow-up. *Scientific Data*, 11(1):988, 2024.

Amir Harati, Meysam Golmohammadi, Silvia Lopez, Iyad Obeid, and Joseph Picone. Improved eeg event classification using differential energy. In *2015 IEEE Signal Processing in Medicine and Biology Symposium (SPMB)*, pp. 1–4. IEEE, 2015.

Kaiming He, Xinlei Chen, Saining Xie, Yanghao Li, Piotr Dollár, and Ross Girshick. Masked autoencoders are scalable vision learners. In *Proceedings of the IEEE/CVF conference on computer vision and pattern recognition*, pp. 16000–16009, 2022.

Cosimo Ieracitano, Nadia Mammone, Alessia Bramanti, Amir Hussain, and Francesco C Morabito. A convolutional neural network approach for classification of dementia stages based on 2d-spectral representation of eeg recordings. *Neurocomputing*, 323:96–107, 2019.

Wei-Bang Jiang, Yansen Wang, Bao-Liang Lu, and Dongsheng Li. Neurolm: A universal multi-task foundation model for bridging the gap between language and eeg signals. *arXiv preprint arXiv:2409.00101*, 2024a.

Wei-Bang Jiang, Li-Ming Zhao, and Bao-Liang Lu. Large brain model for learning generic representations with tremendous eeg data in bci. *arXiv preprint arXiv:2405.18765*, 2024b.

Jin Jing, Wendong Ge, Shenda Hong, Marta Bento Fernandes, Zhen Lin, Chaoqi Yang, Sungtae An, Aaron F Struck, Aline Herlopian, Ioannis Karakis, et al. Development of expert-level classification of seizures and rhythmic and periodic patterns during eeg interpretation. *Neurology*, 100(17):e1750–e1762, 2023.

Min-jae Kim, Young Chul Youn, and Joonki Paik. Deep learning-based eeg analysis to classify normal, mild cognitive impairment, and dementia: Algorithms and dataset. *NeuroImage*, 272:120054, 2023.

Alexander Kirillov, Eric Mintun, Nikhila Ravi, Hanzi Mao, Chloe Rolland, Laura Gustafson, Tete Xiao, Spencer Whitehead, Alexander C Berg, Wan-Yen Lo, et al. Segment anything. In *Proceedings of the IEEE/CVF international conference on computer vision*, pp. 4015–4026, 2023.

Gayal Kuruppu, Neeraj Wagh, and Yogatheesan Varatharajah. Eeg foundation models: A critical review of current progress and future directions. *arXiv preprint arXiv:2507.11783*, 2025.

Vernon J Lawhern, Amelia J Solon, Nicholas R Waytowich, Stephen M Gordon, Chou P Hung, and Brent J Lance. Eegnet: a compact convolutional neural network for eeg-based brain–computer interfaces. *Journal of neural engineering*, 15(5):056013, 2018.

Hongli Li, Man Ding, Ronghua Zhang, and Chunbo Xiu. Motor imagery eeg classification algorithm based on cnn-lstm feature fusion network. *Biomedical signal processing and control*, 72:103342, 2022.

Hongqi Li, Yitong Chen, Yujuan Wang, Weihang Ni, and Haodong Zhang. Foundation models for cross-domain eeg analysis application: A survey. *arXiv preprint arXiv:2508.15716*, 2025.

Wei Liu, Jie-Lin Qiu, Wei-Long Zheng, and Bao-Liang Lu. Comparing recognition performance and robustness of multimodal deep learning models for multimodal emotion recognition. *IEEE Transactions on Cognitive and Developmental Systems*, 2021.

Wei Liu, Wei-Long Zheng, Ziyi Li, Si-Yuan Wu, Lu Gan, and Bao-Liang Lu. Identifying similarities and differences in emotion recognition with eeg and eye movements among chinese, german, and french people. *Journal of Neural Engineering*, 19(2):026012, 2022.

Weiheng Lu, Chunfeng Song, Jiamin Wu, Pengyu Zhu, Yuchen Zhou, Weijian Mai, Qihao Zheng, and Wanli Ouyang. Unimind: Unleashing the power of llms for unified multi-task brain decoding. *arXiv preprint arXiv:2506.18962*, 2025.

- Jingying Ma, Feng Wu, Qika Lin, Yucheng Xing, Chenyu Liu, Ziyu Jia, and Mengling Feng. Codebrain: Bridging decoupled tokenizer and multi-scale architecture for eeg foundation model. *arXiv preprint arXiv:2506.09110*, 2025.
- Andreas Miltiadous, Katerina D Tzimourta, Theodora Afrantou, Panagiotis Ioannidis, Nikolaos Grigoriadis, Dimitrios G Tsalikakis, Pantelis Angelidis, Markos G Tsipouras, Euripidis Glavas, Nikolaos Giannakeas, et al. A dataset of scalp eeg recordings of alzheimer's disease, frontotemporal dementia and healthy subjects from routine eeg. *Data*, 8(6):95, 2023.
- Iyad Obeid and Joseph Picone. The temple university hospital eeg data corpus. *Frontiers in neuroscience*, 10:196, 2016.
- Wei Yan Peh, Yuanyuan Yao, and Justin Dauwels. Transformer convolutional neural networks for automated artifact detection in scalp eeg. In *2022 44th Annual International Conference of the IEEE Engineering in Medicine & Biology Society (EMBC)*, pp. 3599–3602. IEEE, 2022.
- G. Pfurtscheller and C. Neuper. Motor imagery and direct brain-computer communication. *Proceedings of the IEEE*, 89(7):1123–1134, 2001. doi: 10.1109/5.939829.
- Alec Radford, Jong Wook Kim, Chris Hallacy, Aditya Ramesh, Gabriel Goh, Sandhini Agarwal, Girish Sastry, Amanda Askell, Pamela Mishkin, Jack Clark, et al. Learning transferable visual models from natural language supervision. In *International conference on machine learning*, pp. 8748–8763. PMLR, 2021.
- Arman Savran¹, Koray Ciftci¹, Guillame Chanel, Javier Cruz Mota, Luong Hong Viet, Bülent Sankur¹, Lale Akarun¹, Alice Caplier, and Michele Rombaut. Emotiondetection in the loop from brain signals and facial images. 2006.
- Yonghao Song, Xueyu Jia, Lie Yang, and Longhan Xie. Transformer-based spatial-temporal feature learning for eeg decoding. *arXiv preprint arXiv:2106.11170*, 2021.
- Yonghao Song, Qingqing Zheng, Bingchuan Liu, and Xiaorong Gao. Eeg conformer: Convolutional transformer for eeg decoding and visualization. *IEEE Transactions on Neural Systems and Rehabilitation Engineering*, 31:710–719, 2022.
- Logan Trujillo. Raw EEG Data, 2020. URL <https://doi.org/10.18738/T8/SS2NHB>.
- Logan T Trujillo, Candice T Stanfield, and Ruben D Vela. The effect of electroencephalogram (eeg) reference choice on information-theoretic measures of the complexity and integration of eeg signals. *Frontiers in neuroscience*, 11:425, 2017.
- Hanneke Van Dijk, Guido Van Wingen, Damiaan Denys, Sebastian Olbrich, Rosalinde Van Ruth, and Martijn Arns. The two decades brainclinics research archive for insights in neurophysiology (tdbrain) database. *Scientific data*, 9(1):333, 2022.
- Eva von Weltin, Tameem Ahsan, Vinit Shah, Dawer Jamshed, Meysam Golmohammadi, Iyad Obeid, and Joseph Picone. Electroencephalographic slowing: A primary source of error in automatic seizure detection. In *2017 IEEE signal processing in medicine and biology symposium (SPMB)*, pp. 1–5. IEEE, 2017.
- Guangyu Wang, Wenchao Liu, Yuhong He, Cong Xu, Lin Ma, and Haifeng Li. Eegpt: Pretrained transformer for universal and reliable representation of eeg signals. *Advances in Neural Information Processing Systems*, 37:39249–39280, 2024a.
- Jiquan Wang, Sha Zhao, Zhiling Luo, Yangxuan Zhou, Haiteng Jiang, Shijian Li, Tao Li, and Gang Pan. Cbramod: A criss-cross brain foundation model for eeg decoding. *arXiv preprint arXiv:2412.07236*, 2024b.
- Pengfei Wang, Huanran Zheng, Silong Dai, Yiqiao Wang, Xiaotian Gu, Yuanbin Wu, and Xiaoling Wang. A survey of spatio-temporal eeg data analysis: from models to applications. *arXiv preprint arXiv:2410.08224*, 2024c.
- Wei Xiong, Jiangtong Li, Jie Li, and Kun Zhu. Eeg-fm-bench: A comprehensive benchmark for the systematic evaluation of eeg foundation models. *arXiv preprint arXiv:2508.17742*, 2025.

- Chaoqi Yang, M Westover, and Jimeng Sun. Biot: Biosignal transformer for cross-data learning in the wild. *Advances in Neural Information Processing Systems*, 36:78240–78260, 2023a.
- Chaoqi Yang, Cao Xiao, M Brandon Westover, and Jimeng Sun. Self-supervised electroencephalogram representation learning for automatic sleep staging: model development and evaluation study. *JMIR AI*, 2(1):e46769, 2023b.
- Zhizhang Yuan, Fanqi Shen, Meng Li, Yuguo Yu, Chenhao Tan, and Yang Yang. Brainwave: A brain signal foundation model for clinical applications. *arXiv preprint arXiv:2402.10251*, 2024.
- W. Zheng, W. Liu, Y. Lu, B. Lu, and A. Cichocki. Emotionmeter: A multimodal framework for recognizing human emotions. *IEEE Transactions on Cybernetics*, pp. 1–13, 2018. ISSN 2168-2267. doi: 10.1109/TCYB.2018.2797176.
- Wei-Long Zheng and Bao-Liang Lu. Investigating critical frequency bands and channels for eeg-based emotion recognition with deep neural networks. *IEEE Transactions on autonomous mental development*, 7(3):162–175, 2015.
- Xinliang Zhou, Chenyu Liu, Zhisheng Chen, Kun Wang, Yi Ding, Ziyu Jia, and Qingsong Wen. Brain foundation models: A survey on advancements in neural signal processing and brain discovery, 2025a. URL <https://arxiv.org/abs/2503.00580>.
- Yuchen Zhou, Jiamin Wu, Zichen Ren, Zhouheng Yao, Weiheng Lu, Kunyu Peng, Qihao Zheng, Chunfeng Song, Wanli Ouyang, and Chao Gou. Csbrain: A cross-scale spatiotemporal brain foundation model for eeg decoding. *arXiv preprint arXiv:2506.23075*, 2025b.
- Igor Zyma, Sergii Tukaev, Ivan Seleznov, Ken Kiyono, Anton Popov, Mariia Chernykh, and Oleksii Shpenkov. Electroencephalograms during mental arithmetic task performance. *Data*, 4(1):14, 2019.

A RELATED WORK

A.1 MOTIVATION FOR BRAIN FOUNDATION MODELS

Traditional models for electroencephalography (EEG) decoding were mainly task-specific, leading to several core limitations that motivated the shift towards foundation models. These challenges include (Kuruppu et al., 2025; Xiong et al., 2025; Wang et al., 2024c): **1) Poor Generalizability:** Models trained for a specific task, dataset, or individual struggled to transfer knowledge to new contexts. **2) Data Heterogeneity:** EEG data varies significantly across studies in terms of electrode configurations, signal lengths, and sampling rates, creating barriers to cross-dataset learning. **3) Expensive Annotation:** Labeling EEG data requires significant domain expertise and is time-consuming, making large-scale supervised datasets scarce. To overcome these issues, researchers have turned to developing Brain Foundation Models (BFMs), which learn universal and transferable neural representations through self-supervised pre-training on large, diverse datasets (Li et al., 2025; Babu et al., 2025; Aristimunha et al., 2025).

A.2 INNOVATIONS IN BRAIN FOUNDATION MODELS

Existing BFMs have advanced the field through innovations in architecture and pre-training strategies, primarily centered around self-supervised learning.

A.2.1 RECONSTRUCTION-BASED PRE-TRAINING

This paradigm, inspired by masked autoencoders, is the most common approach. Models are trained to reconstruct masked portions of the EEG signal. **LaBraM** (Jiang et al., 2024b) pioneered the use of a vector-quantized neural tokenizer to convert continuous EEG signals into discrete neural codes. By pre-training the model to predict these masked codes, it effectively mitigates signal noise. It has been applied to tasks such as abnormal detection and emotion recognition. **EEGPT** (Wang et al., 2024a) introduced a dual self-supervised learning strategy that combines masked reconstruction with spatio-temporal representation alignment. Instead of reconstructing the raw signal, it aligns the features of masked segments with those of the complete signal, thereby improving representation quality. **BrainWave** (Yuan et al., 2024) is the first foundation model jointly pre-trained on both invasive (iEEG) and non-invasive (EEG) neural signals. It has demonstrated strong zero-shot and few-shot classification abilities in the diagnosis and identification of various neurological disorders. **CBraMod** (Wang et al., 2024b) employs a crisscross transformer backbone to model the EEG signals by processing spatial and temporal dependencies in parallel and uses an asymmetric conditional positional encoding to adapt to diverse EEG formats. It has been evaluated on over 10 BCI tasks, including emotion recognition and seizure detection.

A.2.2 ARCHITECTURES TAILORED TO EEG STRUCTURE

CSBrain (Zhou et al., 2025b) addresses the intrinsic crossscale nature of EEG signals by introducing Cross-scale Spatiotemporal Tokenization and Structured Sparse Attention. This design explicitly models neural patterns at multiple resolutions to suit diverse task requirements. **CodeBrain** (Ma et al., 2025) introduces a TFDual-Tokenizer to independently encode temporal and frequency components. Its backbone is an efficient State Space Model designed to capture the sparse, long-range dependencies characteristic of brain.

A.2.3 DOMAIN-SPECIFIC AND LLM-INTEGRATED MODELS

NeuroLM (Jiang et al., 2024a) and **UniMind** (Lu et al., 2025) are pioneering models that integrate EEG encoders with Large Language Models (LLMs) to create unified, multi-task decoders that operate via instruction tuning. To bridge the significant modality gap, **NeuroLM** uses adversarial training to align EEG and text embedding spaces, while **UniMind** designs a Neuro-Language Connector and a Task-aware Query Selection module to distill neural patterns into LLM-interpretable representations. These models are applied to a wide range of tasks including sleep staging and clinical event classification .

B THE USE OF LARGE LANGUAGE MODELS(LLMs)

During the preparation of this manuscript, we used Google’s Gemini, as a writing-assistance tool. The use of the LLM was strictly limited to improving the language and readability of our text. Key applications included:

- Proofreading for grammatical errors, spelling mistakes, and incorrect punctuation.
- Rephrasing sentences to enhance clarity and conciseness.
- Ensuring a consistent and formal academic tone throughout the document.

Crucially, the LLM was not used for any core scientific aspects of this work. All conceptual contributions, including the formulation of the research problem, the development of the methodology, and the execution of experiments, are exclusively the work of the human authors. The authors have reviewed and edited all text, and take full responsibility for the scientific integrity and final content of this paper.

C DESCRIPTIONS OF EVALUATION METRICS

In a classification context, a confusion matrix is used to visualize the performance of an algorithm. For a binary classification problem, the matrix consists of four fundamental quantities:

- **True Positives (TP):** The number of positive instances that were correctly classified as positive.
- **True Negatives (TN):** The number of negative instances that were correctly classified as negative.
- **False Positives (FP):** The number of negative instances that were incorrectly classified as positive. This is also known as a Type I error.
- **False Negatives (FN):** The number of positive instances that were incorrectly classified as negative. This is also known as a Type II error.

Based on these four values, we can define several key evaluation metrics.

DETAILED EVALUATION METRICS

C.1 BALANCED ACCURACY

Balanced Accuracy is the arithmetic mean of the recall for each class. It is particularly useful for datasets with imbalanced class distributions as it avoids inflated performance estimates.

For a problem with C classes, the recall for class i is first calculated as:

$$\text{Recall}_i = \frac{\text{TP}_i}{\text{TP}_i + \text{FN}_i} \quad (17)$$

where TP_i and FN_i are the true positives and false negatives for class i , respectively.

The Balanced Accuracy is then computed by averaging these recall values:

$$\text{Balanced Accuracy} = \frac{1}{C} \sum_{i=1}^C \text{Recall}_i = \frac{1}{C} \sum_{i=1}^C \frac{\text{TP}_i}{\text{TP}_i + \text{FN}_i} \quad (18)$$

C.2 AUROC (AREA UNDER THE RECEIVER OPERATING CHARACTERISTIC CURVE)

The AUROC metric evaluates a model’s ability to distinguish between classes across all possible classification thresholds. The ROC curve is a plot of the True Positive Rate (TPR) against the False

Positive Rate (FPR).

$$\text{TPR (Sensitivity)} = \frac{\text{TP}}{\text{TP} + \text{FN}} \quad (19)$$

$$\text{FPR (1 - Specificity)} = \frac{\text{FP}}{\text{FP} + \text{TN}} \quad (20)$$

Mathematically, the area under this curve is calculated by integrating the TPR function with respect to the FPR:

$$\text{AUROC} = \int_0^1 \text{TPR}(\text{FPR}) d(\text{FPR}) \quad (21)$$

AUROC is the area under this curve, with a value ranging from 0 to 1. A value of 1 indicates a perfect classifier, while 0.5 suggests performance no better than random chance.

C.3 AUC-PR (AREA UNDER THE PRECISION-RECALL CURVE)

The AUC-PR metric is the area under the curve that plots Precision against Recall at various thresholds.

$$\text{Precision} = \frac{\text{TP}}{\text{TP} + \text{FP}} \quad (22)$$

$$\text{Recall} = \frac{\text{TP}}{\text{TP} + \text{FN}} \quad (23)$$

The area is computed by integrating the precision function $P(r)$ with respect to recall r :

$$\text{AUC-PR} = \int_0^1 P(r) dr \quad (24)$$

This metric is especially informative for imbalanced datasets, as its calculation does not depend on the number of True Negatives. A higher AUC-PR value indicates better model performance.

C.4 COHEN'S KAPPA (κ)

Cohen's Kappa coefficient (κ) measures the agreement between a classifier's predictions and the ground truth, correcting for the probability of agreement occurring by chance. It is a more robust metric than simple accuracy on imbalanced datasets. The formula is:

$$\kappa = \frac{p_o - p_e}{1 - p_e} \quad (25)$$

where:

- p_o is the observed agreement (i.e., overall accuracy):

$$p_o = \frac{\text{TP} + \text{TN}}{\text{TP} + \text{TN} + \text{FP} + \text{FN}}$$

- p_e is the expected probability of chance agreement. For a binary case, it is calculated as:

$$p_e = \frac{(\text{TP} + \text{FP})(\text{TP} + \text{FN}) + (\text{FN} + \text{TN})(\text{FP} + \text{TN})}{(\text{Total Samples})^2}$$

C.5 F1-SCORE

The F1-Score is the harmonic mean of Precision and Recall. It provides a single score that balances both concerns, making it a useful metric when both false positives and false negatives are important.

$$F_1 = 2 \cdot \frac{\text{Precision} \cdot \text{Recall}}{\text{Precision} + \text{Recall}} = \frac{2\text{TP}}{2\text{TP} + \text{FP} + \text{FN}} \quad (26)$$

D PSEUDOCODE

D.1 DETAILED EXPLANATION OF HETEROGENEOUS FEATURE PROJECTION MODEL

Algorithm 1 Heterogeneous Feature Projection Model

Input: preprocessed EEG data $X \in \mathbb{R}^{B \times R \times E \times T}$
Output: three feature sequence matrices $H_T, H_F, H_R \in \mathbb{R}^{B \times L \times T}$

```

1:  $X_{\text{reshaped}} \leftarrow \text{reshape}(X, (B \cdot L, T))$  ▷  $L = R \times E$ 
2: Initialize  $H_T, H_F, H_R$  as empty lists
3: for all  $i \in \{1, \dots, B \cdot L\}$  do
4:    $x_i \leftarrow X_{\text{reshaped}}[i, :]$ 
5:    $h_{i,T} \leftarrow \Phi_T(x_i)$  ▷ Dynamics Waveform Encoder (Time Path)
6:    $P_b(x_i) \leftarrow \text{CalculateBandPower}(x_i)$ 
7:    $h_{i,F} \leftarrow \Phi_F(P_b(x_i))$  ▷ Frequency Decomposition Encoder (Frequency Path)
8:    $h_{i,R} \leftarrow \Phi_R(x_i)$  ▷ Standard Projection Encoder (Raw Path)
9:   Append  $h_{i,T}, h_{i,F}, h_{i,R}$  to  $H_T, H_F, H_R$  respectively
10: end for
11:  $H_T, H_F, H_R \leftarrow \text{stack and reshape each list to } \mathbb{R}^{B \times L \times D}$ 
12: return  $H_T, H_F, H_R$ 

```

Input X : with dimensions $X \in \mathbb{R}^{B \times R \times E \times T}$, where B is the batch size, R is the number of regions, E is the number of electrodes per region, and T is the number of time steps.

Line 1: Reshape Data This step reshapes the original 4D tensor X into a 2D matrix. It merges the region (R) and electrode (E) dimensions into a new dimension L and flattens the batch (B) dimension into it. This is done to treat the time series of each electrode as an independent sample, facilitating subsequent individual processing.

$$X_{\text{reshaped}} \in \mathbb{R}^{(B \cdot L) \times T}, \quad \text{where } L = R \times E \quad (27)$$

After reshaping, we obtain $B \times L$ independent time-series sequences, each of length T .

Lines 3-10: Iterative Feature Extraction The algorithm iterates through all $B \times L$ time-series sequences, performing three independent feature encoding steps for each sequence $x_i \in \mathbb{R}^T$:

1) **TEMPORAL FEATURE EXTRACTION (LINE 5)** The time series x_i is imported into a Dynamics Waveform Encoder Φ_T . This encoder is typically a neural network designed to capture the dynamic characteristics of the signal in the time domain.

$$h_{i,T} = \Phi_T(x_i), \quad \text{where } \Phi_T : \mathbb{R}^T \rightarrow \mathbb{R}^D \quad (28)$$

It maps the sequence of length T to a feature vector $h_{i,T}$ of dimension D .

2) **FREQUENCY FEATURE EXTRACTION (LINES 6-7)** This process is divided into two steps. First, the “CalculateBandPower” function computes the power of the time series x_i across N_b pre-defined frequency bands (e.g., δ, θ, α). After obtaining the band power vector p_i , it is fed into the Frequency Decomposition Encoder Φ_F .

$$p_i = \text{CalculateBandPower}(x_i), \quad p_i \in \mathbb{R}^{N_b} \quad (29)$$

$$h_{i,F} = \Phi_F(p_i), \quad \text{where } \Phi_F : \mathbb{R}^{N_b} \rightarrow \mathbb{R}^D \quad (30)$$

This process results in a feature vector $h_{i,F}$ of dimension D .

3) **STANDARD FEATURE EXTRACTION (LINE 8)** The original time series x_i is also passed to a third, independent Standard Projection Encoder Φ_R . This encoder can use a different network architecture from Φ_T to provide a complementary feature perspective.

$$h_{i,R} = \Phi_R(x_i), \quad \text{where } \Phi_R : \mathbb{R}^T \rightarrow \mathbb{R}^D \quad (31)$$

The output is also a feature vector $h_{i,R}$ of dimension D .

Line 11: Stack and Reshape After the loop completes, the three lists of representations are stacked into matrices of shape $(B \cdot L) \times D$ and then reshaped into the final tensor shape of $\mathbb{R}^{B \times L \times D}$, restoring the batch dimension.

D.2 DETAILED EXPLANATION OF TOPOLOGICAL EMBEDDING

Algorithm 2 Topological Embedding

Require: Temporal, frequency, and standard features $H_T, H_F, H_R \in \mathbb{R}^{B \times L \times D}$
Ensure: Temporal-frequency-topological features $H_{in} \in \mathbb{R}^{B \times L \times D}$

- 1: $I_{region} \leftarrow \text{Generate Region Indices}(B, L, R, E)$
 - 2: $I_{intra} \leftarrow \text{Generate Intra Region Indices}(B, L, R, E)$
 - 3: $I_{abs} \leftarrow \text{torch.arange}(L).expand(B, -1)$
 - 4: $E_{region_emb} \leftarrow \mathbf{E}_{region}[I_{region}]$
 - 5: $E_{intra_emb} \leftarrow \mathbf{E}_{intra}[I_{intra}]$
 - 6: $E_{abs_emb} \leftarrow \mathbf{E}_{abs}[I_{abs}]$
 - 7: $H_{in} \leftarrow H_{fused} + H_R + E_{region_emb} + E_{intra_emb} + E_{abs_emb}$
 - 8: **return** H_{in}
-

Lines 1-3: Generate Positional Indices The algorithm first generates three types of integer indices, all resulting in tensors of shape (B, L) , to encode the spatial hierarchy of the electrodes:

- I_{region} : **Region Index**, which identifies the brain region $(0, \dots, R - 1)$ that each of the L electrodes belongs to.
- I_{intra} : **Intra-Region Index**, which indicates the relative position $(0, \dots, E - 1)$ of an electrode within its specific region.
- I_{abs} : **Absolute Position Index**, which gives the absolute position $(0, \dots, L - 1)$ of each electrode in the flattened sequence.

For any given electrode at absolute position $j \in \{0, \dots, L - 1\}$, its indices are formally generated as:

$$I_{region}^{(j)} = \lfloor j/E \rfloor \quad (32)$$

$$I_{intra}^{(j)} = j \pmod{E} \quad (33)$$

where $\lfloor \cdot \rfloor$ is the floor operation and \pmod{E} gives the remainder of a division by E .

Lines 4-6: Lookup Embeddings Using the generated indices, the algorithm retrieves corresponding feature vectors from three distinct, learnable embedding matrices. This process maps the discrete integer indices to dense, continuous vector representations. The learnable matrices are:

- $\mathbf{E}_{region} \in \mathbb{R}^{R \times D}$: An embedding matrix for the R brain regions.
- $\mathbf{E}_{intra} \in \mathbb{R}^{E \times D}$: An embedding matrix for the E intra-region positions.
- $\mathbf{E}_{abs} \in \mathbb{R}^{L \times D}$: An embedding matrix for the L absolute positions.

The lookup operation for an electrode at absolute position j can be expressed as:

$$E_{region_emb}^{(j)} = \mathbf{E}_{region}[I_{region}^{(j)}] \quad (34)$$

This operation is performed for all indices and all three embedding matrices, resulting in three embedding tensors (E_{region_emb} , E_{intra_emb} , E_{abs_emb}), each of shape $\mathbb{R}^{B \times L \times D}$.

Line 7: Final Feature Fusion Finally, the algorithm performs an element-wise addition to combine the time-frequency fused features (H_{fused}), the standard projection features (H_R), and the three structural prior embeddings.

$$H_{in} = H_{fused} + H_R + E_{region_emb} + E_{intra_emb} + E_{abs_emb} \quad (35)$$

The result, H_{in} , is a unified representation that incorporates temporal, frequency, raw signal, and spatial information, ready for a downstream model.

E DATASETS

Table 6 provides a detailed record of the nine public EEG datasets used to construct the large-scale pre-training corpus, a critical prerequisite for training a universal foundation model. The table not only lists basic parameters such as the name, sampling rate, and channel count for each dataset but also highlights the diversity of their origins in the “Description” column. This includes recordings from resting-state conditions (e.g., REEG-BACA), emotion induction tasks (e.g., Emobrain, SEED-series), and large-scale clinical data (e.g., TUEG, CAUEEG). This significant heterogeneity in recording equipment, experimental paradigms, and subject populations provides a robust data foundation for the model to learn truly generalizable and resilient neural representations.

Table 6: Information of datasets used for pre-training.

Dataset	Rate (Hz)	Channels	Time (H)	Subjects	Description
Emobrain (Savran et al., 2006)	1024	64	4.94	16	The multimodal emotion dataset contains recordings from 16 participants. Emotional states were induced by presenting the subjects with a curated selection of stimuli from the International Affective Picture System (IAPS) dataset.
REEG-BACA (Getzmann et al., 2024)	1000	64	121.6	608	The dataset is composed of 64-channel resting-state EEG recordings from an initial cohort of 608 participants, of whom 61.8% were female, with an age range of 20 to 70 years. Furthermore, a longitudinal component of the study involved follow-up measurements for 208 of these participants.
SEED-series (Zheng et al., 2018 ; Liu et al., 2021; 2022)	1000	62	170.54	51	This series includes SEED-IV, SEED-V, SEED-GER, and SEED-FRA, with subject counts of 15, 20, 8, and 8, respectively.
CAUEEG (Kim et al., 2023)	200	19	306	1388	The CAUEEG dataset is recorded at Chung-Ang University Hospital from August 24, 2012, to March 12, 2020. All recordings adhered to the International 10-20 system, utilizing a linked earlobe referencing method.
TUEG (Obeid & Picone, 2016)	250-1024	17-23	27100	14987	Temple University Hospital EEG corpus has over 40 distinct channel setups and inconsistent recording lengths, and most data use sampling frequency of 256 Hz.
Raw EEG Data (Trujillo, 2020)	256	64	34.35	—	Datasets are in BioSemi Data Format (BDF), which were recorded during the reported Information-Integration categorization task and reported multidimensional Rule-Based categorization task.
BCI Competition IV-1 (Blankertz et al., 2007)	1000	59	8.21	7	The EEG data were acquired using multi-channel amplifiers, sampled at 1000 Hz, and band-pass filtered from 0.05 to 200 Hz.
Resting State EEG Data (Trujillo et al., 2017)	256	64	3.04	22	A total of 22 undergraduate students from Texas State University (11 female, 11 male; mean age: 21.1 ± 0.52 years; age range: 18–26) took part in this research.
Siena Scalp EEG Database (Dettì et al., 2020)	512	31	30.47	14	Data for this study were sourced from 14 epileptic subjects, whose cerebral activity was recorded via video scalp EEG. The signals were sampled at 512 Hz, and the electrodes were arranged according to the international 10–20 system.

Table 7 serves as the core reference for validating the generalization abilities of the Uni-NTFM model, systematically organizing the nine benchmark datasets used for downstream task evaluation. To comprehensively assess the model’s performance, the selected tasks cover a range of important domains from clinical diagnostics to Brain-Computer Interfaces, such as TUAB for abnormal EEG detection, TDBrain for psychiatric disorder classification, and BCIC-IV-2a for motor imagery recognition. The table clearly specifies the dataset for each task, the number of subjects, and the clas-

Table 7: Information of datasets used for downstream evaluation.

Task	Dataset	Rate (Hz)	Channels	Subjects	Label
Abnormal Detection	TUAB (Harati et al., 2015)	256	23	2,383	2-class
Event Type Classification	TUEV (Harati et al., 2015)	256	23	370	6-class
Emotion Recognition	SEED (Zheng & Lu, 2015)	1000	62	16	5-class
Psychiatric Dysfunction Classification	TDBrain (Van Dijk et al., 2022)	500	26	1274	2-class
Neurodegenerative Disorder Classification	ADFTD (Miltiadous et al., 2023)	500	19	65	3-class
Motor Imagery Classification	BCIC-IV-2a (Brunner et al., 2008)	250	22	9	4-class
Cognitive Workload Classification	Workload (Zyma et al., 2019)	500	19	36	2-class
Sleep Staging	HMC (Alvarez-Estevez & Rijssman, 2021)	256	4	151	5-class
Slowing Event Classification	TUSL (von Weltin et al., 2017)	256	23	28	3-class

sification target (number of labels), providing a clear context for the rigorous evaluation protocols, which include both Linear Probing and full Fine-tuning.

F MODEL SETTINGS OF DIFFERENT SCALES

Table 8 offers a detailed configuration settings for the four core Uni-NTFM model variants designed in this research, demonstrating the progressive scaling from the 57M-parameter Uni-NTFM_{*tiny*} to the 1.9B-parameter Uni-NTFM_{*large*}. It clearly outlines the differences in key architectural parameters among the variants, including embedding dimension, Transformer network depth, and the number of experts in the MoE module. Furthermore, the table specifies the base hyperparameters, such as learning rate, optimizer weight decay, and gradient clipping threshold, to ensure a fair comparison between models of different scales and to support the reproducibility of the experiments.

Table 8: Configurations and hyperparameters for different variants of Uni-NTFM.

Settings	Uni-NTFM _{<i>tiny</i>}	Uni-NTFM _{<i>small</i>}	Uni-NTFM _{<i>middle</i>}	Uni-NTFM _{<i>large</i>}
Model size	57M	427M	912M	1.9B
Emb_dim *	256	512	512	768
Transformer depth	12	12	26	24
Number of experts	8	16	16	16
Batch size	128	128	64	32
Numbers of GPU	16	16	16	32
GPU	NVIDIA A100-SXM4-80G			
Number of regions	5			
Sequence of length	1600			
Dropout ratio	0.1			
Mask ratio	0.25			
Number of frequency bands	5			
Frequency loss weight	0.2			
Time loss weight	0.8			
Learning rate	3e-5			
Weight decay	1e-4			
Total epochs	50			
Warmup epochs	5			
Gradient clipping	1.0			
Use AMP	True			

* Emb.dim refers to Transformer Embedding dimension.

Table 9, 10, 11 collectively form the detailed technical appendix for the model scaling law experiments, ensuring the transparency and reproducibility of this part of the research. They systematically record the precise architectural settings for a series of twelve models ranging in size from 10M to 1B parameters. Readers can clearly observe how key parameters like embedding dimension, Transformer depth, and the number of experts were carefully adjusted to achieve specific model sizes. This series of detailed configurations ensures that the investigation into the relationship between model performance and parameter count was conducted under controlled and systematic conditions.

Table 9: Configurations and hyperparameters for $10M \sim 200M$ of Uni-NTFM.

Settings	Uni-NTFM _{size1}	Uni-NTFM _{size2}	Uni-NTFM _{size3}	Uni-NTFM _{size4}
Model size	10M	50M	100M	200M
Emb.dim *	128	256	256	256
Transformer depth	8	10	16	32
Number of experts	8	8	12	16
Batch size	128	128	128	128
Numbers of GPU	4	4	4	4
GPU	NVIDIA A100-SXM4-80G			
Number of regions	5			
Sequence of length	1600			
Dropout ratio	0.1			
Mask ratio	0.25			
Number of frequency bands	5			
Frequency loss weight	0.2			
Time loss weight	0.8			
Learning rate	3e-5			
Weight decay	1e-4			
Total epochs	50			
Warmup epochs	5			
Gradient clipping	1.0			
Use AMP	True			

* Emb.dim refers to Transformer Embedding dimension.

Table 10: Configurations and hyperparameters for $300M \sim 600M$ of Uni-NTFM.

Settings	Uni-NTFM _{size5}	Uni-NTFM _{size6}	Uni-NTFM _{size7}	Uni-NTFM _{size8}
Model size	300M	400M	500M	600M
Emb.dim *	512	512	512	512
Transformer depth	11	11	14	17
Number of experts	12	16	16	16
Batch size	128	128	128	128
Numbers of GPU	8	8	8	8
GPU	NVIDIA A100-SXM4-80G			
Number of regions	5			
Sequence of length	1600			
Dropout ratio	0.1			
Mask ratio	0.25			
Number of frequency bands	5			
Frequency loss weight	0.2			
Time loss weight	0.8			
Learning rate	3e-5			
Weight decay	1e-4			
Total epochs	50			
Warmup epochs	5			
Gradient clipping	1.0			
Use AMP	True			

* Emb.dim refers to Transformer Embedding dimension.

Table 11: Configurations and hyperparameters for $700M \sim 1B$ of Uni-NTFM.

Settings	Uni-NTFM _{size9}	Uni-NTFM _{size10}	Uni-NTFM _{size11}	Uni-NTFM _{size12}
Model size	700M	800M	900M	1B
Emb.dim *	512	512	512	768
Transformer depth	20	23	26	13
Number of experts	16	16	16	16
Batch size	64	64	64	64
Numbers of GPU	8	8	8	8
GPU	NVIDIA A100-SXM4-80G			
Number of regions	5			
Sequence of length	1600			
Dropout ratio	0.1			
Mask ratio	0.25			
Number of frequency bands	5			
Frequency loss weight	0.2			
Time loss weight	0.8			
Learning rate	3e-5			
Weight decay	1e-4			
Total epochs	50			
Warmup epochs	5			
Gradient clipping	1.0			
Use AMP	True			

* Emb.dim refers to Transformer Embedding dimension.

G DETAILED RESULTS OF SCALING LAW

To systematically discuss the impact of model and data scale on the performance of Uni-NTFM, we conducted two controlled scaling law experiments. The specific configurations for each model and other detailed hyperparameter settings are provided in Table 9, 10, 11. The results visualized in Figure 3 intuitively demonstrate that the representational quality of Uni-NTFM scales positively with both the number of model parameters and the volume of pre-training data. The detailed data results are shown in Table 12 and 13.

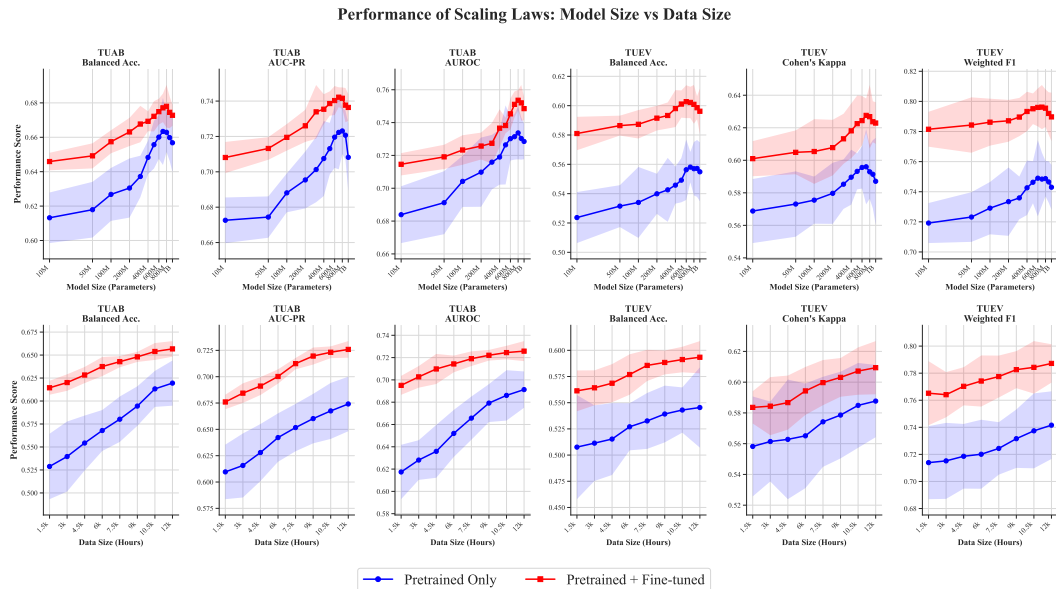


Figure 3: This figure shows the scaling laws of the Uni-NTFM model, revealing a positive correlation between performance and both model size and data volume. The top row of plots indicates that with a fixed pre-training data size, model performance steadily improves as the number of parameters increases. The bottom row shows that for a fixed model size, performance also scales positively with more of pre-training data. All plots contrast the performance under “Pretrained Only” (blue curve) and “Pretrained - Fine-tuned” (red curve) evaluation settings.

1) Impact of Model Size: We first evaluated the effect of model scale by training models ranging from approximately 10M to 1B parameters on a fixed pre-training corpus of 10,000 hours. As shown in Table 12, downstream performance on both TUAB and TUEV tasks exhibits a clear and positive relationship with model size. Specifically, in the fine-tuned setting on the TUAB task, the AUROC score consistently improves from 0.7146 for the 10M model to a peak of 0.7536 for the 800M model. This trend holds across all metrics for both linear probing and fine-tuning detection, confirming that larger models can learn more powerful and universal representations. However, performance appears to saturate and slightly reduce for models larger than 800M, suggesting that the corpus of 10,000 hours may be insufficient to fully release the potential of models with billion-parameter.

2) Impact of Data Size: We fixed the model size to our 57M parameter variant (Uni-NTFM_{tiny}) and varied the pre-training corpus from 1,500 to 12,000 hours. The results in Figure 3 and Table 13 indicate a strong dependence of performance on data size. On the TUEV task, for example, the fine-tuned Balanced Accuracy steadily increases from 0.5613 with 1,500 hours of data to 0.5934 with 12,000 hours. The performance curves do not show signs of saturation, indicating that even the smaller 57M model could benefit from further pre-training on a larger corpus.

Table 12 presents the core experimental data from the scaling law analysis, focusing on the impact of model size. It quantitatively demonstrates the specific performance of Uni-NTFM on the TUAB and TUEV downstream tasks as its parameter count increases from approximately 10M to 1B. The data clearly show that, in both linear probing and fine-tuning settings, larger models generally learn more powerful universal representations, as reflected by the steady improvement across most evaluation

metrics. The data in this table also reveal an interesting phenomenon: performance slightly saturates or declines when model size exceeds 800M, and we infer that the training corpus may be insufficient to fully unlock the potential of the largest models.

Table 12: Quantitative analysis of the impact of model size on TUAB and TUEV.

Model Size	TUAB (2-class)			TUEV (6-class)		
	Balanced Acc.	AUC-PR	AUROC	Balanced Acc.	Cohen's Kappa	Weighted F1
<i>Only Pretrained Foundation Models (Multi-tasks)</i>						
10,301,200 (~10M)	0.6132 \pm 0.0147	0.6726 \pm 0.0129	0.6839 \pm 0.0173	0.5237 \pm 0.0174	0.5688 \pm 0.0197	0.7192 \pm 0.0133
48,335,760 (~50M)	0.6179 \pm 0.0162	0.6744 \pm 0.0117	0.6912 \pm 0.0192	0.5315 \pm 0.0143	0.5731 \pm 0.0201	0.7232 \pm 0.0165
108,808,592 (~100M)	0.6268 \pm 0.0154	0.6881 \pm 0.0110	0.7042 \pm 0.0156	0.5340 \pm 0.0242	0.5755 \pm 0.0145	0.7291 \pm 0.0174
203,197,584 (~200M)	0.6305 \pm 0.0172	0.6954 \pm 0.0161	0.7098 \pm 0.0211	0.5399 \pm 0.0137	0.5797 \pm 0.0188	0.7334 \pm 0.0227
299,943,056 (~300M)	0.6372 \pm 0.0121	0.7013 \pm 0.0185	0.7159 \pm 0.0166	0.5426 \pm 0.0218	0.5853 \pm 0.0152	0.7359 \pm 0.0142
392,352,912 (~400M)	0.6483 \pm 0.0097	0.7075 \pm 0.0212	0.7190 \pm 0.0168	0.5458 \pm 0.0126	0.5896 \pm 0.0169	0.7426 \pm 0.0181
496,317,072 (~500M)	0.6557 \pm 0.0139	0.7131 \pm 0.0146	0.7264 \pm 0.0241	0.5492 \pm 0.0151	0.5932 \pm 0.0111	0.7463 \pm 0.0140
600,281,232 (~600M)	0.6601 \pm 0.0127	0.7196 \pm 0.0174	0.7302 \pm 0.0133	0.5563 \pm 0.0206	0.5956 \pm 0.0130	0.7490 \pm 0.0253
704,245,392 (~700M)	0.6634 \pm 0.0195	0.7223 \pm 0.0209	0.7314 \pm 0.0140	0.5581 \pm 0.0104	0.5960 \pm 0.0231	0.7484 \pm 0.0175
808,209,552 (~800M)	0.6629 \pm 0.0115	0.7231 \pm 0.0131	0.7337 \pm 0.0161	0.5570 \pm 0.0182	0.5929 \pm 0.0166	0.7487 \pm 0.0118
912,173,712 (~900M)	0.6598 \pm 0.0136	0.7207 \pm 0.0140	0.7303 \pm 0.0129	0.5572 \pm 0.0194	0.5914 \pm 0.0210	0.7465 \pm 0.0137
1,035,695,760 (~1B)	0.6568 \pm 0.0170	0.7082 \pm 0.0192	0.7285 \pm 0.0108	0.5549 \pm 0.0201	0.5871 \pm 0.0267	0.7430 \pm 0.0149
<i>Pretrained and Fine-tuned Foundation Models (Single-task)</i>						
10,301,200 (~10M)	0.6459 \pm 0.0051	0.7081 \pm 0.0088	0.7146 \pm 0.0068	0.5810 \pm 0.0114	0.6010 \pm 0.0108	0.7815 \pm 0.0116
48,335,760 (~50M)	0.6492 \pm 0.0073	0.7132 \pm 0.0064	0.7191 \pm 0.0074	0.5864 \pm 0.0068	0.6049 \pm 0.0135	0.7843 \pm 0.0184
108,808,592 (~100M)	0.6574 \pm 0.0067	0.7195 \pm 0.0075	0.7233 \pm 0.0090	0.5873 \pm 0.0097	0.6054 \pm 0.0199	0.7862 \pm 0.0156
203,197,584 (~200M)	0.6631 \pm 0.0082	0.7260 \pm 0.0091	0.7257 \pm 0.0082	0.5915 \pm 0.0084	0.6078 \pm 0.0171	0.7871 \pm 0.0139
299,943,056 (~300M)	0.6677 \pm 0.0106	0.7339 \pm 0.0152	0.7274 \pm 0.0124	0.5933 \pm 0.0089	0.6132 \pm 0.0154	0.7896 \pm 0.0127
392,352,912 (~400M)	0.6693 \pm 0.0058	0.7354 \pm 0.0085	0.7366 \pm 0.0115	0.5980 \pm 0.0126	0.6181 \pm 0.0168	0.7933 \pm 0.0131
496,317,072 (~500M)	0.6722 \pm 0.0088	0.7386 \pm 0.0069	0.7382 \pm 0.0047	0.6011 \pm 0.0093	0.6225 \pm 0.0173	0.7951 \pm 0.0102
600,281,232 (~600M)	0.6749 \pm 0.0075	0.7403 \pm 0.0082	0.7453 \pm 0.0095	0.6027 \pm 0.0112	0.6244 \pm 0.0152	0.7960 \pm 0.0126
704,245,392 (~700M)	0.6771 \pm 0.0083	0.7422 \pm 0.0056	0.7511 \pm 0.0079	0.6022 \pm 0.0107	0.6276 \pm 0.0104	0.7962 \pm 0.0147
808,209,552 (~800M)	0.6780 \pm 0.0124	0.7416 \pm 0.0061	0.7536 \pm 0.0062	0.6009 \pm 0.0132	0.6268 \pm 0.0195	0.7955 \pm 0.0125
912,173,712 (~900M)	0.6745 \pm 0.0092	0.7377 \pm 0.0097	0.7520 \pm 0.0109	0.5986 \pm 0.0079	0.6237 \pm 0.0126	0.7920 \pm 0.0141
1,035,695,760 (~1B)	0.6728 \pm 0.0061	0.7364 \pm 0.0076	0.7485 \pm 0.0071	0.5962 \pm 0.0155	0.6229 \pm 0.0128	0.7897 \pm 0.0161

Table 13: Quantitative analysis of the impact of data size on performance.

Data Size	TUAB (2-class)			TUEV (6-class)		
	Balanced Acc.	AUC-PR	AUROC	Balanced Acc.	Cohen's Kappa	Weighted F1
<i>Only Pretrained Foundation Models (Multi-tasks)</i>						
~1500H	0.5288 \pm 0.0356	0.6096 \pm 0.0259	0.6174 \pm 0.0244	0.5076 \pm 0.0497	0.5582 \pm 0.0325	0.7139 \pm 0.0270
~3000H	0.5396 \pm 0.0381	0.6157 \pm 0.0304	0.6281 \pm 0.0178	0.5114 \pm 0.0361	0.5614 \pm 0.0260	0.7152 \pm 0.0281
~4500H	0.5543 \pm 0.0299	0.6280 \pm 0.0271	0.6359 \pm 0.0237	0.5153 \pm 0.0343	0.5628 \pm 0.0389	0.7186 \pm 0.0239
~6000H	0.5679 \pm 0.0223	0.6422 \pm 0.0230	0.6520 \pm 0.0211	0.5270 \pm 0.0225	0.5651 \pm 0.0340	0.7201 \pm 0.0255
~7500H	0.5802 \pm 0.0247	0.6517 \pm 0.0225	0.6657 \pm 0.0194	0.5326 \pm 0.0267	0.5742 \pm 0.0293	0.7244 \pm 0.0194
~9000H	0.5945 \pm 0.0215	0.6602 \pm 0.0235	0.6792 \pm 0.0170	0.5392 \pm 0.0271	0.5786 \pm 0.0282	0.7316 \pm 0.0216
~10500H	0.6132 \pm 0.0196	0.6675 \pm 0.0266	0.6861 \pm 0.0226	0.5430 \pm 0.0216	0.5849 \pm 0.0276	0.7374 \pm 0.0277
~12000H	0.6195 \pm 0.0246	0.6741 \pm 0.0259	0.6913 \pm 0.0163	0.5454 \pm 0.0383	0.5877 \pm 0.0235	0.7416 \pm 0.0250
<i>Pretrained and Fine-tuned Foundation Models (Single-task)</i>						
~1500H	0.6144 \pm 0.0076	0.6760 \pm 0.0069	0.6951 \pm 0.0085	0.5613 \pm 0.0195	0.5836 \pm 0.0105	0.7652 \pm 0.0237
~3000H	0.6201 \pm 0.0090	0.6844 \pm 0.0093	0.7027 \pm 0.0097	0.5642 \pm 0.0167	0.5844 \pm 0.0189	0.7641 \pm 0.0167
~4500H	0.6283 \pm 0.0088	0.6911 \pm 0.0085	0.7098 \pm 0.0135	0.5686 \pm 0.0182	0.5867 \pm 0.0176	0.7703 \pm 0.0141
~6000H	0.6375 \pm 0.0104	0.7002 \pm 0.0068	0.7143 \pm 0.0075	0.5769 \pm 0.0193	0.5943 \pm 0.0156	0.7742 \pm 0.0189
~7500H	0.6428 \pm 0.0061	0.7124 \pm 0.0054	0.7190 \pm 0.0066	0.5856 \pm 0.0149	0.5997 \pm 0.0147	0.7775 \pm 0.0155
~9000H	0.6480 \pm 0.0055	0.7196 \pm 0.0081	0.7221 \pm 0.0048	0.5884 \pm 0.0114	0.6031 \pm 0.0126	0.7826 \pm 0.0137
~10500H	0.6539 \pm 0.0092	0.7232 \pm 0.0056	0.7245 \pm 0.0061	0.5912 \pm 0.0122	0.6072 \pm 0.0154	0.7843 \pm 0.0194
~12000H	0.6567 \pm 0.0085	0.7259 \pm 0.0079	0.7258 \pm 0.0090	0.5934 \pm 0.0154	0.6094 \pm 0.0173	0.7872 \pm 0.0142

Table 13 complements the scaling law analysis by validating its other critical dimension: the importance of data volume. With the model size fixed to the 57M-parameter Uni-NTFM_{tiny} variant, the table documents how model performance on the TUAB and TUEV tasks evolves as the amount of pre-training data increases from approximately 1,500 to 12,000 hours. The results show a clear and consistent upward trend in performance with more data, for both linear probing and fine-tuning evaluations.

H T-SNE VISUALIZATION OF LEARNED FEATURE REPRESENTATIONS

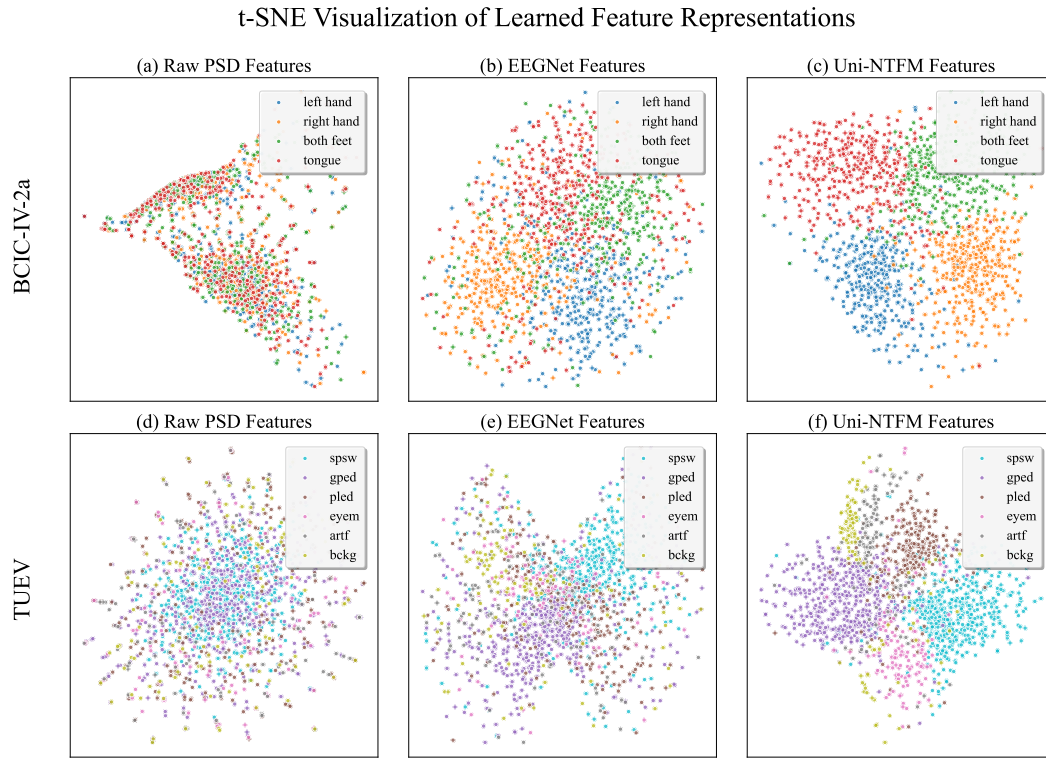


Figure 4: t-SNE Visualization of Learned Feature Representations. This figure provides a qualitative comparison of feature spaces learned on the BCIC-IV-2a (top row) and TUEV (bottom row) datasets. The columns represent features from different sources: (a, d) Raw Power Spectral Density (PSD) features, which serve as a baseline; (b, e) features extracted from a trained EEGNet model, representing a standard deep learning approach; and (c, f) features from our only pre-trained Uni-NTFM model. Each color corresponds to a distinct class within the respective dataset. The clear formation of well-separated and compact clusters in the rightmost column (c, f) visually demonstrates Uni-NTFM’s superior ability to learn discriminative and generalizable neural representations.

To provide a qualitative and intuitive assessment of our model’s representation learning abilities, we employed the t-SNE dimensionality reduction technique to visualize the learned feature spaces. Figure 4 shows this analysis on two distinct downstream tasks: the 4-class motor imagery task (BCIC-IV-2a) and the more complex 6-class clinical event detection task (TUEV).

As expected, (a, d) exhibit no discernible class structure, with points from all classes aggregated in a single and messy cloud. This establishes the inherent difficulty of separating these classes directly from traditional features. The middle column (b, e) shows the feature space after processing by a trained, task-specific EEGNet model. They remain diffuse and suffer from significant overlap at their boundaries. This indicates that while standard deep learning architectures can learn some useful patterns, they struggle to create truly separable representations, especially for the more challenging TUEV dataset.

In contrast, the column (c, f) shows the feature space learned by our pre-trained Uni-NTFM. Even for the challenging 6-class TUEV task, Uni-NTFM effectively disentangles the different clinical event types into distinct regions of the feature space. This visual evidence corroborates our quantitative results, confirming that the paradigm of Uni-NTFM enables it to learn far more powerful and generalizable representations than standard methods.